



Galaxy Cluster Pressure Profiles as Determined by Sunyaev Zel'dovich Effect Observations with MUSTANG and Bolocam. II. Joint Analysis of 14 Clusters

Charles E. Romero^{1,13}, Brian S. Mason², Jack Sayers³, Tony Mroczkowski^{4,5}, Craig Sarazin⁶, Megan Donahue⁷, Alessandro Baldi⁷, Tracy E. Clarke⁵, Alexander H. Young⁸, Jonathan Sievers⁹, Simon R. Dicker¹⁰, Erik D. Reese¹¹, Nicole Czakon^{3,12}, Mark Devlin¹⁰, Phillip M. Korngut³, and Sunil Golwala³

¹ Institut de Radioastronomie Millimétrique 300 rue de la Piscine, Domaine Universitaire F-38406 Saint Martin d'Hères, France; romero@iram.fr

² National Radio Astronomy Observatory, 520 Edgemont Road, Charlottesville, VA 22903, USA

³ Department of Physics, Math, and Astronomy, California Institute of Technology, Pasadena, CA 91125, USA

⁴ ESO—European Organization for Astronomical Research in the Southern Hemisphere, Karl-Schwarzschild-Str. 2, D-85748 Garching b. München, Germany

⁵ U.S. Naval Research Laboratory, 4555 Overlook Avenue SW, Washington, DC 20375, USA

⁶ Department of Astronomy, University of Virginia, P.O. Box 400325, Charlottesville, VA 22904, USA

⁷ Physics and Astronomy Department, Michigan State University, 567 Wilson Road, East Lansing, MI 48824, USA

⁸ MIT Lincoln Laboratories, 244 Wood Street Lexington, MA 02421-6426, USA

⁹ Astrophysics & Cosmology Research Unit, University of KwaZulu-Natal, Private Bag X54001, Durban 4000, South Africa

¹⁰ Department of Physics and Astronomy, University of Pennsylvania, 209 South 33rd Street, Philadelphia, PA, 19104, USA

¹¹ Department of Physics, Astronomy, and Engineering, Moorpark College, 7075 Campus Rd., Moorpark, CA 93021, USA

¹² Academia Sinica, 128 Academia Road, Nankang, Taipei 115, Taiwan

Received 2016 August 5; revised 2017 February 23; accepted 2017 February 28; published 2017 March 29

Abstract

We present pressure profiles of galaxy clusters determined from high-resolution Sunyaev–Zel'dovich (SZ) effect observations of 14 clusters, which span the redshift range of $0.25 < z < 0.89$. The procedure simultaneously fits spherical cluster models to MUSTANG and Bolocam data. In this analysis, we adopt the generalized NFW parameterization of pressure profiles to produce our models. Our constraints on ensemble-average pressure profile parameters, in this study γ , C_{500} , and P_0 , are consistent with those in previous studies, but for individual clusters we find discrepancies with the X-ray derived pressure profiles from the ACCEPT2 database. We investigate potential sources of these discrepancies, especially cluster geometry, electron temperature of the intracluster medium, and substructure. We find that the ensemble mean profile for all clusters in our sample is described by the parameters $[\gamma, C_{500}, P_0] = [0.3_{-0.1}^{+0.1}, 1.3_{-0.1}^{+0.1}, 8.6_{-2.4}^{+2.4}]$, cool core clusters are described by $[\gamma, C_{500}, P_0] = [0.6_{-0.1}^{+0.1}, 0.9_{-0.1}^{+0.1}, 3.6_{-1.5}^{+1.5}]$, and disturbed clusters are described by $[\gamma, C_{500}, P_0] = [0.0_{-0.0}^{+0.1}, 1.5_{-0.2}^{+0.1}, 13.8_{-1.6}^{+1.6}]$. Of the 14 clusters, 4 have clear substructure in our SZ observations, while an additional 2 clusters exhibit potential substructure.

Key words: galaxies: clusters: general – galaxies: clusters: intracluster medium

1. Introduction

Galaxy clusters are the largest gravitationally bound objects in the universe and thus serve as excellent cosmological probes and astrophysical laboratories. Within a galaxy cluster, the gas in the intracluster medium (ICM) constitutes 90% of the baryonic mass (Vikhlinin et al. 2006) and is directly observable in the X-ray due to bremsstrahlung emission. At millimeter and submillimeter wavelengths, the ICM is observable via the Sunyaev–Zel'dovich (SZ) effect (Sunyaev & Zel'dovich 1972): the inverse Compton scattering of cosmic microwave background (CMB) photons off of the hot ICM electrons. The thermal SZ is observed as an intensity decrement relative to the CMB at wavelengths longer than ~ 1.4 mm (frequencies less than ~ 220 GHz). The amplitude of the thermal SZ is proportional to the integrated line-of-sight electron pressure, and is often parameterized as Compton y : $y = (\sigma_T/m_e c^2) \int P_e dl$, where σ_T is the Thomson cross-section, m_e is the electron mass, c is the speed of light, and P_e is the electron pressure.

Cosmological constraints derived from galaxy cluster samples are generally limited by the accuracy of mass calibration of galaxy clusters (e.g., Hasselfield et al. 2013; Reichardt et al. 2013), which is often calculated via a scaling

relation with respect to some integrated observable quantity. Scatter in the scaling relations will then depend on the regularity of clusters and the adopted integration radius of the clusters. Determining pressure profiles of galaxy clusters provides an assessment of the relative impact and frequency of various astrophysical processes in the ICM and can refine the choice of integration radius of galaxy clusters to reduce the scatter in scaling relations.

In the core of a galaxy cluster, some observed astrophysical processes include shocks and cold fronts (e.g., Markevitch & Vikhlinin 2007), sloshing (e.g., Fabian et al. 2006), and X-ray cavities (McNamara & Nulsen 2007). It is also theorized that helium sedimentation should occur, most noticeably in low-redshift, dynamically relaxed clusters (Abramopoulos et al. 1981; Gilfanov & Syunyaev 1984) and recently the expected helium enhancement via sedimentation has been numerically simulated (Peng & Nagai 2009). This would result in an offset between X-ray and SZ derived pressure profiles if not accounted for correctly.

At large radii ($R \gtrsim R_{500}$),¹⁴ equilibration timescales are longer, accretion is ongoing, and hydrostatic equilibrium (HSE) can be a poor approximation. Several numerical simulations

¹³ Grote Reber Fellow.

¹⁴ R_{500} is the radius at which the enclosed average mass density is 500 times the critical density, $\rho_c(z)$, of the universe.

Table 1
Cluster Properties

Cluster	z	M_{500} ($10^{14} M_{\odot}$)	P_{500} (keV cm $^{-3}$)	R_{500} (kpc)	R_{500} (')	T_x^a (keV)	T_x^b (keV)	T_{mg} (keV)	Dynamical state	$\Delta r_{X,\text{SZ}}$ (')
Abell 1835	0.253	12	0.00594	1490	6.30	9.0	10.0	7.49	CC	6.8
Abell 611	0.288	7.4	0.00445	1240	4.75	6.8	...	6.71	...	18.7
MACS 1115	0.355	8.6	0.00545	1280	4.28	9.2	9.14	7.04	CC	34.8
MACS 0429	0.399	5.8	0.00448	1100	3.41	8.3	8.55	5.56	CC	18.7
MACS 1206	0.439	19	0.01059	1610	4.73	10.7	11.4	10.0	...	6.9
MACS 0329	0.450	7.9	0.00596	1190	3.44	6.3	5.85	5.64	CC & D	14.8
RXJ1347	0.451	22	0.01171	1670	4.83	10.8	13.6	9.86	CC	9.6
MACS 1311	0.494	3.9	0.00399	930	2.56	6.0	6.36	5.18	CC	27.7
MACS 1423	0.543	6.6	0.00612	1090	2.85	6.9	6.81	5.50	CC	19.8
MACS 1149	0.544	19	0.01228	1530	4.01	8.5	8.76	7.70	D	6.0
MACS 0717	0.546	25	0.01490	1690	4.40	11.8	10.6	9.06	D	32.4
MACS 0647	0.591	11	0.00923	1260	3.17	11.5	12.6	8.06	...	6.9
MACS 0744	0.698	13	0.01199	1260	2.96	8.1	8.90	6.85	D	4.9
CLJ1226	0.888	7.8	0.01184	1000	2.15	12.0	11.7	11.3	...	15.3

Note. z , M_{500} , R_{500} , and T_x^a are taken from Mantz et al. (2010): T_x^a is calculated from a single spectrum over $0.15R_{500} < r < R_{500}$ for each cluster. T_x^b is from Morandi et al. (2015), and is calculated over $0.15R_{500} < r < 0.75R_{500}$. T_{mg} is a fitted gas mass weighted temperature, (Section 6.2) determined by fitting the ACCEPT2 (Baldi 2014) temperature profiles to the gas mass weighted profile found in Vikhlinin et al. (2006). The dynamical states: cool core (CC) and disturbed (D) are taken from (and defined in) Sayers et al. (2013a). $\Delta r_{X,\text{SZ}}$ denotes the offset between the ACCEPT and Bolocam centroids.

show that the fractional contribution from non-thermal pressure increases with radius (Shaw et al. 2010; Battaglia et al. 2012; Nelson et al. 2014). For all three studies, non-thermal pressure fractions between 15% and 30% are found at ($R \sim R_{500}$) for redshifts $0 < z < 1$. Additionally, clumping is expected to increase with radius (Kravtsov & Borgani 2012), and is expected to increase the scatter of pressure profiles at large radii (Nagai & Lau 2011) as well as biasing X-ray derived gas density high, and thus X-ray derived thermal pressure low (Battaglia et al. 2015).

By contrast, the intermediate region, between the core and outer regions of the galaxy cluster, is often the best region to apply self-similar scaling relations derived from HSE (e.g., Kravtsov & Borgani 2012). Moreover, both simulations and observations find low cluster-to-cluster scatter in pressure profiles within this intermediate radial range (e.g., Borgani et al. 2004; Nagai et al. 2007; Arnaud et al. 2010; Bonamente et al. 2012; Planck Collaboration et al. 2013; Sayers et al. 2013a).

In recent years, the SZ community has often adopted the pressure profile presented in Arnaud et al. (2010; hereafter, A10), who derive their pressure profiles from X-ray data from the REXCESS sample of 31 nearby ($z < 0.2$) clusters out to R_{500} and numerical simulations for larger radii. The adoption of the A10 pressure profile allows for the extraction of an integrated observable quantity which, via scaling relations, can then be used to determine the mass of the clusters. In this paper, we use high-resolution SZ data to test the validity of this pressure profile in our sample of 14 clusters at intermediate redshifts.

There are many existing facilities capable of making SZ observations, but most have angular resolutions of one arcminute or larger. The MUSTANG camera (Dicker et al. 2008) on the 100 meter Robert C. Byrd Green Bank Telescope (GBT, Jewell & Prestage 2004) with its angular resolution of $9''$ (full-width, half-maximum FWHM) is one of only a few SZ effect instruments with sub-arcminute resolution. However, MUSTANG's instantaneous field of view (FOV) of $42''$ means

that it is not sensitive to scales over $\sim 1'$. To probe a wider range of scales, we complement our MUSTANG data with SZ data from Bolocam (Glenn et al. 1998). Bolocam is a 144-element bolometer array on the Caltech Submillimeter Observatory (CSO) with a beam FWHM of $58''$ at 140 GHz and circular FOV with $8'$ diameter, which is well matched to the angular size of R_{500} ($\sim 4'$) of the clusters in our sample.

This paper is organized as follows. In Section 2, we describe the MUSTANG and Bolocam observations and reduction. In Section 3, we review the method used to jointly fit pressure profiles to MUSTANG and Bolocam data. We present results from the joint fits in Section 4 and compare our results to X-ray derived pressures in Section 6. Throughout this paper, we assume a Λ CDM cosmology with $\Omega_m = 0.3$, $\Omega_\lambda = 0.7$, and $H_0 = 70 \text{ km s}^{-1} \text{ Mpc}^{-1}$. For the remainder of the paper, we denote the electron pressure as P , electron density as n_e , and electron temperature as T . The errors we report are 1σ (68.5% confidence) unless otherwise noted.

2. Observations and Data Reduction

2.1. Sample

Our cluster sample is based primarily on the Cluster Lensing And Supernova survey with Hubble (CLASH) sample (Postman et al. 2012). The CLASH sample has 25 massive galaxy clusters, 20 of which are selected from X-ray data (from *Chandra X-ray Observatory*, hereafter *Chandra*), and 5 are based on exceptional lensing strength. These clusters have the following properties: $0.187 < z < 0.890$, $5.5 < k_B T$ (keV) < 15.5 , and $6.7 \times 10^{44} < L_{\text{bol}}$ (erg s $^{-1}$) < 90.8 . Thus, these clusters are large enough that we should expect to detect them with MUSTANG with a reasonable amount of time on the sky (on average, < 25 hr per cluster).

Of the 25 clusters in the CLASH sample, 4 are too far south to be observed with MUSTANG from Green Bank, WV. Of the remaining 21, we were able to observe 14 given the available good weather and their limited visibility during the observational campaign from 2009 to 2014. Abell 209 was observed,

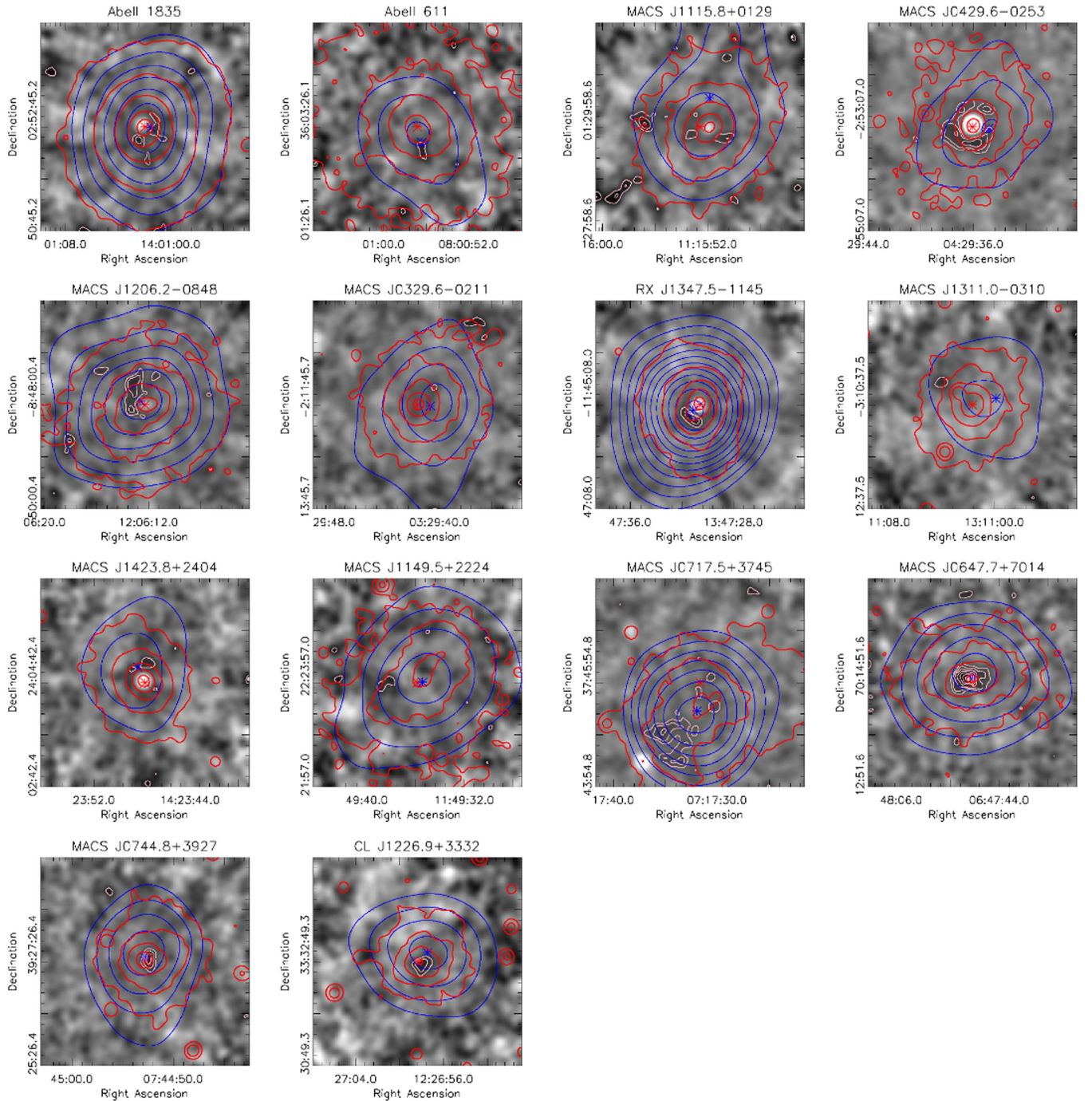


Figure 1. The grayscale shows MUSTANG maps of the clusters in our sample, in Jy/beam. The color scaling spans the range of $\pm 5 \times \text{Noise}_M$, where Noise_M (for MUSTANG) is given in Table 2. Pale contours are MUSTANG contours; blue contours are Bolocam. Both start at a 3σ decrement (i.e., negative), with 1σ intervals for MUSTANG and 2σ intervals for Bolocam. Red contours are X-ray surface brightness contours at arbitrary levels. The red asterisk is the ACCEPT centroid; the blue asterisk is the Bolocam centroid.

but was relatively noisy and showed no trace of any detection. Our final sample includes 13 CLASH clusters. We also include Abell 1835, a cluster of similar mass and redshift as the CLASH clusters, which was observed under the program GBT/09A-052. These clusters (see Table 1 and Figure 1) were also observed with Bolocam, and have been analyzed in Sayers et al. (2012, 2013a) and Czakon et al. (2015). The *Archive of Chandra Cluster Entropy Profile Tables* (ACCEPT Cavagnolo et al. 2009) and Bolocam centroids are indicated in Figure 1 with red and blue asterisks, respectively, and their separations

($\Delta r_{X,SZ}$) are also listed in Table 1. The total integration times of MUSTANG and Bolocam observations, along with detection significances, of our sample are listed in Table 2. Bolocam and MUSTANG significances, $A10_B$ and $A10_M$, respectively, are taken as the significance of the fitted spherical A10 (Arnaud et al. 2010) profile (see Section 3.2.1) based on the amplitude of the fit (P_0/σ_{P_0}) to the respective data set (separately). Aside from fixing the pressure profile shape, the fits are performed as described in Section 3, with relevant (point source and/or residual) components fit simultaneously. This calculation of

Table 2
Bolocam and MUSTANG Observational Properties

Cluster	z	R.A. (J2000)	Decl. (J2000)	$t_{\text{obs},B}$ (hr)	Noise _{<i>B</i>} μK^a	A10 _{<i>B</i>} (P_0/σ_{P_0})	$\bar{\chi}_B^2$	$t_{\text{obs},M}$ (hr)	Noise _{<i>M</i>} $\mu Jy/bm$	A10 _{<i>M</i>} (P_0/σ_{P_0})	$\bar{\chi}_M^2$
Abell 1835	0.253	14:01:01.9	+02:52:40	14.0	16.2	28.9	1.05	8.6	53.4	10.0	0.99
Abell 611	0.288	08:00:56.8	+36:03:26	18.7	25.0	13.9	0.97	12.0	46.2	1.73	1.03
MACS 1115	0.355	11:15:51.9	+01:29:55	15.7	22.8	16.3	1.08	10.0	56.4	8.66	1.04
MACS 0429	0.399	04:29:36.0	−02:53:06	17.0	24.1	13.2	1.05	11.6	47.2	−0.02	1.03
MACS 1206	0.439	12:06:12.3	−08:48:06	11.3	24.9	28.7	0.97	13.3	42.5	8.89	1.02
MACS 0329	0.450	03:29:41.5	−02:11:46	10.3	22.5	17.4	1.09	13.1	39.9	8.63	0.98
RXJ1347	0.451	13:47:30.8	−11:45:09	15.5	19.7	45.3	1.04	1.9	276.	8.90	0.98
MACS 1311	0.494	13:11:01.7	−03:10:40	14.2	22.5	11.3	1.06	10.6	64.5	0.71	1.00
MACS 1423	0.543	14:23:47.9	+24:04:43	21.7	22.3	11.8	0.88	11.2	35.7	6.15	1.00
MACS 1149	0.544	11:49:35.4	+22:24:04	17.7	24.0	22.0	0.99	13.9	32.7	−1.47	1.01
MACS 0717	0.546	07:17:32.1	+37:45:21	12.5	29.4	31.3	1.09	14.6	27.1	3.05	1.05
MACS 0647	0.591	06:47:49.7	+70:14:56	11.7	22.0	24.1	1.03	16.4	20.3	11.3	1.01
MACS 0744	0.698	07:44:52.3	+39:27:27	16.3	20.6	17.8	1.19	7.6	48.5	7.67	1.01
CLJ1226	0.888	12:26:57.9	+33:32:49	11.8	22.9	13.7	1.20	4.9	85.6	9.43	1.00

Note. Subscripts B and M denote Bolocam and MUSTANG properties respectively. Noise_{*B*} and $t_{\text{obs},B}$ are those reported in Sayers et al. (2013a). Noise_{*M*} is calculated on MUSTANG maps with $10''$ smoothing, in the central arcminute. t_{obs} are the integration times (on source) for the given instruments. A10_{*B*} and A10_{*M*} are the Bolocam and MUSTANG significances, respectively. The quality of the fits is respectable, as indicated by the $\bar{\chi}^2$ values being close to 1.

^a μK is more precisely $\mu K_{\text{CMB-amin}}$.

cluster significance is better than a peak surface brightness measure because it incorporates signal, even if weak, within the entire fitted region. As this metric is intended to measure the strength of an overall cluster detection, negative values are permitted. Null detections with MUSTANG set upper limits on the slope of the inner pressure profile, which are stronger than those from Bolocam data.

2.2. MUSTANG Observations and Reduction

MUSTANG is a 64 pixel array of Transition Edge Sensor (TES) bolometers arranged in an 8×8 array located at the Gregorian focus on the 100 m GBT. Operating at 90 GHz (81–99 GHz), MUSTANG has an angular resolution of $9''$ and pixel spacing of $0.63f\lambda$ resulting in an FOV of $42''$. More detailed information about the instrument can be found in Dicker et al. (2008).

Our observations and data reduction are described in detail in Romero et al. (2015), and we briefly review them here. Absolute flux calibrations are based on the planets Mars, Uranus, and Saturn, or the star Betelgeuse ($\alpha_{\text{Or}}i$). At least one of these flux calibrators was observed at least once per night, and we find that our calibration is accurate to a 10% rms uncertainty. We also observe bright point sources every half hour to track our pointing and beam shape. To observe the target galaxy clusters, we employ Lissajous daisy scans with a $3'$ radius and in many of the clusters we broadened our coverage with a hexagonal pattern of daisy centers (with $1'$ offsets). For most clusters, the coverage (weight) drops to 50% of its peak value at a radius of 1.3 .

Processing of MUSTANG data is performed using a custom IDL pipeline. Raw data is recorded as time ordered data (TOD) from each of the 64 detectors. An outline of the data processing for each scan on a galaxy cluster is as follows.

1. We define a pixel mask from the nearest preceding CAL scan; unresponsive detectors are masked out. The CAL scan provides us with unique gains to be applied to each of the responsive detectors.

2. A common mode template, polynomial, and sinusoid are fit to the data and then subtracted. The common mode is calculated as the arithmetic mean of the TOD across detectors.
3. After the common mode and polynomial subtraction, each scan is subjected to spike (glitch), skewness, and Allan variance tests and are flagged according to the following criteria. Glitches are flagged as 4σ excursions based on the median absolute deviation; the skewness threshold for flagging is 0.4. Flags based on Allan variance require the variance over a two second interval to be greater than nine times the variance between each integration. Typical scan integration times were 150 s.
4. Individual detector weights are calculated as $1/\sigma_i^2$, where σ_i is the rms of the non-flagged TOD for that detector.
5. Maps are produced by gridding the TOD in $1''$ pixels in right ascension (R.A.) and declination (decl). A weight map is produced in addition to the signal map.

The effect of the MUSTANG data processing results in the transfer function shown in Figure 2. Specifically, it is the average across our sample. This transfer function is very stable because little scatter is seen across our sample.

2.3. Bolocam Observations and Reduction

Bolocam is a 144-element camera that was a facility instrument on the Caltech Submillimeter Observatory (CSO) from 2003 until 2012. Its field of view is $8'$ in diameter, and at 140 GHz it has a resolution of $58''$ FWHM (Glenn et al. 1998; Haig et al. 2004). The clusters were observed with a Lissajous pattern that results in a tapered coverage dropping to 50% of the peak value at a radius of roughly $5'$, and to 0 at a radius of $10'$. The Bolocam maps used in this analysis are $14' \times 14'$. The Bolocam data¹⁵ are the same as those used in Czakon et al. (2015) and Sayers et al. (2013a); the details of the reduction are given therein, along with Sayers et al. (2011). The reduction

¹⁵ Bolocam data is publicly available at http://irsa.ipac.caltech.edu/data/Planck/release_2/ancillary-data/bolocam/.

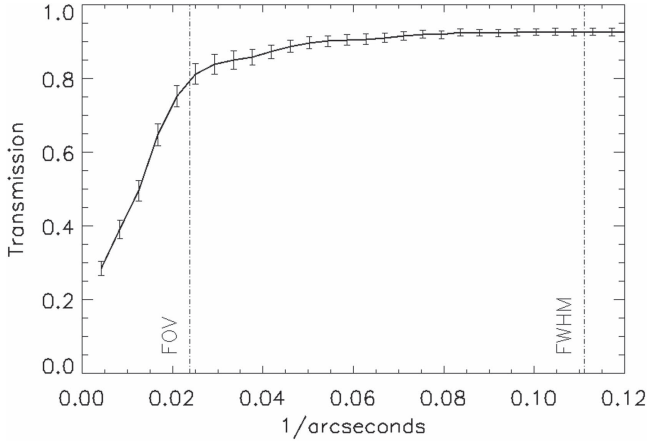


Figure 2. Effective average transfer function of our MUSTANG data reduction over our sample. The variations between clusters are less than 3%. For each cluster, attenuation is calculated based on simulated observations of 25 fake skies. The plotted one-dimensional transfer function is the weighted average of the transfer functions of individual clusters. The error bars show the scatter among cluster transfer functions. The transfer functions (transmission) of individual clusters are calculated as the square root of the ratio of the one-dimensional power spectra of the observed fake sky and input fake sky. We have labelled the relevant angular wavenumbers for the FOV and FWHM.

and calibration is similar to that used for MUSTANG, and Bolocam achieves a 5% calibration accuracy and 5'' pointing accuracy.

3. Joint Map Fitting Technique

3.1. Overview

The joint map fitting technique used in this paper is described in detail in Romero et al. (2015). We review it briefly here. The general approach follows that of a least squares fitting procedure, which assumes that we can make a model map as a linear combination of model components.

This linear combination can be written as

$$\mathbf{d}_{\text{mod}} = \mathbf{A}\mathbf{a}_{\text{mod}}, \quad (1)$$

where \mathbf{d}_{mod} is the total model, each column in \mathbf{A} is a filtered model component (Section 3.2), and \mathbf{a}_{mod} is an array of amplitudes of the components. There are up to four types of components for which we fit: a bulk component, point-source (s), residual component(s), and a mean level. From these, we produce a sky model for the bulk component and point source to be filtered. The residual component is calculated directly as a filtered component.

We wish to fit \mathbf{d}_{mod} to our data, \mathbf{d} , and allow for a calibration offset between Bolocam and MUSTANG data. To accomplish this, we define our data vector as

$$\mathbf{d} = [\mathbf{d}_B, k\mathbf{d}_M, k], \quad (2)$$

where \mathbf{d}_B is the Bolocam data, taken as the provided map (14' sides), \mathbf{d}_M is the MUSTANG data, taken as the inner (radial) arcminute of MUSTANG maps. k is the calibration offset of MUSTANG relative to Bolocam, to which we apply an 11.2% Gaussian prior derived from the MUSTANG and Bolocam calibration uncertainties.

We use the χ^2 statistic as our goodness of fit:

$$\chi^2 = (\vec{d} - \vec{d}_{\text{mod}})^T \mathbf{N}^{-1} (\vec{d} - \vec{d}_{\text{mod}}), \quad (3)$$

where \mathbf{N} is the covariance matrix; however, because we wish to fit for k in addition to the amplitude of model components, we no longer have completely linearly independent variables, and thus we employ MPFIT (Markwardt 2009) to solve for these variables. Confidence intervals are derived from χ^2 values over the parameter space searched (Section 3.3), and adjusted based on Monte Carlo simulations (Romero et al. 2015).

Our approach is to fix the shape and position of point sources and residuals (if any), fitting only their amplitudes. We explore the shape of the bulk ICM component parametrically, where each point in the parametric space may be forward modeled (Section 3.3). At each point in the parameter space, we do a linear least squares fit followed by a nonlinear minimization over k , the Bolocam pointing, and \mathbf{a}_{mod} .

3.2. Components

In order to produce component maps, it is necessary to account for the response of both instruments and imaging pipeline filter functions. For Bolocam, we use the transfer function provided. For MUSTANG, we perform simulated observations, processing the sky models in the same manner that real data is processed.

3.2.1. Bulk ICM

As in Romero et al. (2015), the bulk component is taken to be a spherically symmetric 3D electron pressure profile as parameterized by a generalized Navarro, Frenk, and White profile (hereafter, gNFW Navarro et al. 1997; Nagai et al. 2007):

$$\tilde{P} = \frac{P_0}{(C_{500}X)^\gamma [1 + (C_{500}X)^\alpha]^{(\beta-\gamma)/\alpha}} \quad (4)$$

where $X = R/R_{500}$, and C_{500} is the concentration parameter; one can also write $(C_{500}X)$ as (R/R_s) , where $R_s = R_{500}/C_{500}$. \tilde{P} is the electron pressure in units of the characteristic pressure P_{500} . This pressure profile is integrated along the line of sight to produce a Compton y profile, given as

$$y(r) = \frac{P_{500}\sigma_T}{m_e c^2} \int_{-\infty}^{\infty} \tilde{P}(r, l) dl \quad (5)$$

where $R^2 = r^2 + l^2$, r is the projected radius, and l is the distance from the center of the cluster along the line of sight. Once integrated, $y(r)$ is gridded as $y(\theta)$ and is realized as two maps with the same astrometry as the MUSTANG and Bolocam data maps (pixels of 1'' and 20'' on a side, respectively). In each case, we convolve the Compton y map by the appropriate beam shape. For Bolocam, we use a Gaussian with FWHM = 58'', and for MUSTANG we use the double Gaussian, representing the GBT main beam and stable error beam (Romero et al. 2015). Subsequently, we account for the filtering effects of data processing for each instrument, as described in Romero et al. (2015).

3.2.2. Point Sources

Point sources are treated in the same manner as in Romero et al. (2015). All compact sources in our sample are well

Table 3
Point-source Flux Densities

Cluster	R.A. (J2000)	Decl. (J2000)	S_{90} (mJy)	S_{140} (mJy)
Abell 1835	14:01:02.07	+2:52:47.52	1.37 ± 0.08	0.7 ± 0.2
MACS 1115	11:15:51.82	+1:29:56.82	1.04 ± 0.11	...
MACS 0429	04:29:35.97	-2:53:04.74	7.67 ± 0.84	6.0 ± 1.8
MACS 1206	12:06:12.11	-8:48:00.85	0.75 ± 0.08	...
RXJ1347	13:47:30.61	-11:45:09.48	7.40 ± 0.58	4.0 ± 1.2
MACS 1423	14:23:47.71	+24:04:43.66	1.36 ± 0.13	0.7 ± 0.2
MACS 0717	07:17:37.03	+37:44:24.00	2.08 ± 0.25	...
CLJ1226	12:27:00.01	+33:32:42.00	0.36 ± 0.11	...

Note. S_{90} is the best-fit flux density to MUSTANG, and S_{140} is the extrapolated flux density in the Bolocam maps (at 140 GHz). The location of the point source is reported from the fitted centroid to the MUSTANG data. The conversion from mJy to the equivalent μK_{CMB} is given as $S_{140}(\text{mJy}/\text{bm}) \sim S_{140}/20(\mu\text{K}_{\text{CMB}})$.

modeled as a point source. We clearly detect point sources in Abell 1835, MACS 1115, MACS 0429, MACS 1206, RXJ1347, MACS 1423, and MACS 0717 in the MUSTANG maps. While no point source is evident from our raw MUSTANG map, a point source is identified by NIKA (Adam et al. 2015) in CLJ1226, which is posited to be a submillimeter galaxy (SMG) behind the cluster. That point source is distinct from the point source seen in Korngut et al. (2011), which is not evident in our map. The fitted point source in MACS 0717 is due to a foreground elliptical galaxy and was fit in Mroczkowski et al. (2012); it is not within the central arcminute, our nominal MUSTANG region considered (Section 3.1). Therefore, we extend the fitted region of the MUSTANG map to include the point source in MACS 0717 (see Figure 9). All of the remaining point sources (six) are coincident (within $3''$ of reported coordinates) with the BCGs of their respective clusters (Crawford et al. 1999; Donahue et al. 2015). Moreover, of these six BCGs, four of them exhibit “unambiguous UV excess” (Donahue et al. 2015). The remaining two are Abell 1835 and MACS 1206. The UV excess in MACS 1206 may be due to lensed background systems (Donahue et al. 2015). Abell 1835 is not in the CLASH sample and thus was not included in Donahue et al. (2015). However, it was observed by O’Dea et al. (2010) and found to have a far-UV flux corresponding to a star formation rate of $11.7 M_{\odot}$ per year, which fits within the SFR range of ($5\text{--}80 M_{\odot} \text{ yr}^{-1}$) of the UV excess BCGs found in Donahue et al. (2015). For the Bolocam images, the point sources in Abell 1835, MACS 0429, RXJ1347, and MACS 1423 have been subtracted based on an extrapolation of a power-law fit to the 1.4 GHz NVSS (Condon et al. 1998) and 30 GHz SZA (Bonamente et al. 2012) measurements as detailed in Sayers et al. (2013b); they found that the Bolocam measurements were consistent with a 30% scatter in the extrapolated flux densities from the fits to the lower frequency data. This additional uncertainty is applied to all extrapolated flux densities and accounts for potential breaks in the spectral index. The flux densities for these point sources are shown in Table 3; the MUSTANG flux densities provide support for the extrapolated flux densities at 140 GHz.

3.2.3. Residual Components

Residual components are selected primarily based on peak decrements exceeding 4σ within the central arcminute of

smoothed MUSTANG first-pass residual maps, which are not well fitted by a bulk model. For clarity, any subsequent residual maps (after fitting any residual component described here), are simply referred to as residual maps. We fit residual components for MACS 1206, RXJ 1347, MACS 0717, and MACS 0744. The residual component for MACS 0717 is coincident with subcluster C as identified in Ma et al. (2009), and has a centroid outside the central arcminute, but the features in the MUSTANG map extend into the central arcminute. Although we do not fit for residual components in Abell 611 and MACS 1115, we report properties of potential residual components for these two clusters. We do not fit the residual component for Abell 611 because the peak significance is not 4σ . For MACS 1115, the centroid of the residual component is just outside the central arcminute and does not affect our fit.

To model the shape of residual component, we fit a two-dimensional Gaussian to the selected pixels (those below -3σ). This Gaussian is then fit to the unsmoothed MUSTANG data map (in units of Compton y), with only its amplitude allowed to vary to obtain the results presented in Table 4.

3.2.4. Mean Level

Similar to Czakon et al. (2015), we wish to account for a mean level (signal offset) in the MUSTANG maps. We do not wish to fit for a mean level simultaneously as a bulk component given the degeneracies. Therefore, to determine the mean level independent of the other components, we create a MUSTANG noise map and calculate the mean within the inner arcminute for each cluster. This mean is then subtracted before the other components are fit.

3.3. Parameter Space

As in Romero et al. (2015), we fix MUSTANG’s centroid, but allow Bolocam’s pointing to vary by $\pm 10''$ in R.A. and decl. with a prior on Bolocam’s radial pointing accuracy with an rms uncertainty of $5''$. Our approach to find the absolute calibration offset between Bolocam and MUSTANG is the same as in Romero et al. (2015; see also Section 3.1).

In Romero et al. (2015), we performed a grid search over γ and C_{500} , marginalizing over P_0 , where α and β are fixed to values determined from A10. To determine the impact of our choice of fixed α and β , we explored how the profile shapes change when different, fixed, values of α and β are adopted. In all cases, we find that the pressure profile shapes are in very good agreement with one another and that the differences in χ^2 values are statistically consistent. Thus, our fits are not sensitive to the exact choice of α and β .

We adopt R_{500} from Mantz et al. (2010) and we search over $0 < \gamma < 1.3$ in steps of $\delta\gamma = 0.1$, and over $0.1 < C_{500} < 3.3$ in steps of $\delta C_{500} = 0.1$. This choice of parameter space searched is determined by computation requirements (largely in filtering maps) and covering a sufficient range of values. Our choice to limit $\gamma \geq 0$ is motivated by its implications to hydrostatic equilibrium under thermal pressure support. We revisit this choice in Section 4.1. To create models in finer steps than $\delta\gamma$ and δC_{500} , we interpolate filtered model maps from nearest neighbors from the grid of original filtered models.

All of the gNFW parameters (P_0 , C_{500} , α , β , and γ) have some degeneracy with each other. C_{500} relates the scaling radius, R_s , which is directly constrained by the SZ data, to R_{500}

Table 4
Parameters of Residual Components from MUSTANG

Cluster	R.A. (J2000)	Decl. (J2000)	Modeled Peak y (10^{-5})	FWHM_B ($''$)	FWHM_A ($''$)	θ (deg.)	Fitted Peak y (10^{-5})
Abell 611	8:00:56.20	36:03:00.08	8.4	20.7	35.3	70	...
MACS 1115	11:15:56.66	1:30:02.82	14	17.8	28.8	48	...
MACS 1206	12:06:12.91	-8:47:33.48	7.6	23.5	23.5	155	3.6 ± 0.7
RXJ1347	13:47:31.06	-11:45:18.38	42	12.2	30.1	48	52 ± 9
MACS 0717	7:17:34.01	37:44:49.73	4.4	58.9	58.9	...	4.6 ± 1.1
MACS 0744	7:44:52.22	39:27:28.71	11	17.0	23.5	91	9.0 ± 2.8

Note. Residual components modeled with a two-dimensional Gaussian. θ is measured CCW (going east) from due north. The modeled peak y is the peak when fit to the first-pass residual map, and the fitted peak y is the re-normalized peak when fit, with the other components, to the data map. FWHM_A and FWHM_B correspond to the widths of the major and minor axes, respectively.

Table 5
Summary of Fitted Pressure Profiles

Cluster	R_{500}^a (Mpc)	$Y_{\text{cyl}}(R_{500})$ (10^{-5} Mpc^2)	$Y_{\text{sph}}(R_{500})$ (10^{-5} Mpc^2)	$10^3 P_{500}^a$ keV cm^{-3}	P_0	C_{500}	α	β	γ	k	$\tilde{\chi}^2$	dof
Abell 1835	1.49	$26.75^{+6.05}_{-6.15}$	$21.81^{+4.12}_{-4.49}$	5.94	2.15 ± 0.07	$0.77^{+0.23}_{-0.17}$	1.05	5.49	$0.78^{+0.12}_{-0.13}$	1.08	0.99	12880
Abell 611	1.24	$9.67^{+4.85}_{-2.57}$	$8.73^{+3.68}_{-2.21}$	4.45	35.43 ± 2.46	$2.00^{+0.40}_{-0.30}$	1.05	5.49	$0.00^{+0.15}$	0.96	1.02	12882
MACS 1115	1.28	$30.28^{+7.32}_{-6.30}$	$20.10^{+3.84}_{-3.52}$	5.45	0.67 ± 0.04	$0.35^{+0.15}_{-0.10}$	1.05	5.49	$0.87^{+0.18}_{-0.27}$	1.11	1.04	12875
MACS 0429	1.10	$30.41^{+7.72}_{-6.88}$	$19.57^{+4.00}_{-3.74}$	4.48	11.01 ± 0.77	$0.59^{+0.11}_{-0.09}$	1.05	5.49	$0.00^{+0.15}$	1.00	1.03	12875
MACS 1206	1.61	$61.52^{+12.49}_{-12.63}$	$48.16^{+8.19}_{-8.27}$	10.59	2.39 ± 0.10	$0.74^{+0.16}_{-0.14}$	1.05	5.49	$0.51^{+0.14}_{-0.16}$	1.09	1.01	12874
MACS 0329	1.19	$13.38^{+3.83}_{-2.99}$	$11.86^{+2.93}_{-2.37}$	5.93	9.30 ± 0.50	$1.18^{+0.72}_{-0.28}$	1.05	5.49	$0.41^{+0.19}_{-0.41}$	1.03	0.99	12876
RXJ1347	1.67	$42.47^{+8.29}_{-6.81}$	$37.80^{+5.78}_{-5.11}$	11.71	3.24 ± 0.08	$1.18^{+1.02}_{-0.48}$	1.05	5.49	$0.80^{+0.30}_{-0.70}$	1.15	0.99	12880
MACS 1311	0.93	$17.18^{+3.80}_{-3.49}$	$10.08^{+1.79}_{-1.73}$	3.99	2.75 ± 0.22	$0.35^{+0.15}_{-0.05}$	1.05	5.49	$0.41^{+0.34}_{-0.41}$	0.98	1.00	12881
MACS 1423	1.09	$10.35^{+4.00}_{-2.73}$	$8.89^{+2.53}_{-2.07}$	6.12	22.39 ± 1.71	$1.58^{+0.22}_{-0.48}$	1.05	5.49	$0.00^{+0.35}$	1.04	0.98	12876
MACS 1149	1.53	$56.87^{+8.04}_{-9.00}$	$41.62^{+4.99}_{-5.67}$	12.28	5.50 ± 0.25	$0.83^{+0.07}_{-0.03}$	1.05	5.49	$0.00^{+0.05}$	0.87	1.00	12876
MACS 0717	1.69	$54.16^{+9.56}_{-8.72}$	$48.06^{+7.71}_{-6.95}$	14.90	21.88 ± 0.68	$2.00^{+0.20}_{-0.20}$	1.05	5.49	$0.00^{+0.05}$	0.49	1.03	13583
MACS 0647	1.26	$34.06^{+10.21}_{-7.76}$	$26.33^{+5.37}_{-4.72}$	9.23	2.78 ± 0.11	$0.70^{+0.30}_{-0.20}$	1.05	5.49	$0.60^{+0.15}_{-0.20}$	1.14	1.01	12876
MACS 0744	1.26	$15.10^{+4.50}_{-3.01}$	$13.20^{+3.18}_{-2.29}$	11.99	13.15 ± 0.81	$1.71^{+0.29}_{-0.21}$	1.05	5.49	$0.00^{+0.15}$	0.90	1.02	12875
CLJ1226	1.00	$10.50^{+2.65}_{-1.94}$	$9.46^{+2.03}_{-1.60}$	11.84	19.29 ± 1.25	$1.90^{+0.60}_{-0.50}$	1.05	5.49	$0.29^{+0.36}_{-0.29}$	0.92	1.03	12875
All	8.58 ± 2.37	$1.3^{+0.1}_{-0.1}$	1.05	5.49	$0.3^{+0.1}_{-0.1}$
Cool Core	3.55 ± 1.53	$0.9^{+0.1}_{-0.1}$	1.05	5.49	$0.6^{+0.1}_{-0.1}$
Disturbed	13.81 ± 1.55	$1.6^{+0.1}_{-0.1}$	1.05	5.49	$0.0^{+0.1}$
All (A10)	$8.403h_{70}^{-3/2}$	1.18	1.05	5.49	0.31
Cool core (A10)	$3.249h_{70}^{-3/2}$	1.13	1.22	5.49	0.78
Disturbed (A10)	$3.202h_{70}^{-3/2}$	1.08	1.41	5.49	0.38

Note. Results from our pressure profile analysis. Y_{sph} is calculated using the tabulated value of R_{500} . We have assumed A10 values of α and β . The findings from A10 are reproduced in the last three rows. The h_{70} dependence is included for explicit replication of A10 results; all P_0 values have this dependence (the assumed cosmologies are the same).

^a Values of R_{500} and P_{500} are taken from Mantz et al. (2010) and Sayers et al. (2013a) respectively.

as $R_s = C_{500}R_{500}$. Because we take R_{500} , α , and β from A10, which used X-ray data and numerical simulations to derive their values of α and β , the values constrained by our SZ data in this analysis are not entirely independent of X-ray data. However, given the insensitivity to α and β found in Romero et al. (2015), and the independent nature of R_s , the profile shapes themselves should be considered approximately independent from X-ray data, if not the constrained shape parameter values as well.

3.3.1. Centroid Choice

The default centroids used when gridding our bulk ICM component are the ACCEPT centroids. Given the offsets between ACCEPT and Bolocam centroids (Table 1), we perform a second set of fits where we grid the bulk ICM

component using the Bolocam centroids and we do not find significant changes in the fitted gNFW parameters (Section 4). The ACCEPT centroids are taken to be the X-ray peaks unless the centroiding algorithm produced a centroid more than 70 kpc from the X-ray peak, in which case they adopt that centroid (Cavagnolo et al. 2008).

3.4. Robustness of the Joint Fitting Technique

Our goodness of fits are tabulated as reduced χ^2 in Table 5. The residual MUSTANG and Bolocam maps indicate that a spherically symmetric gNFW pressure profile provides an adequate description of the data. In several residual MUSTANG maps, especially for those clusters with $\tilde{\chi}^2 > 1.02$, some 3σ features remain (within the fitted region). MUSTANG residuals in MACS 1115 and MACS 0717, which have

significances beyond 4σ , are well away from the X-ray cluster centroid and nearly outside of the fitted region. Thus, these residuals will not impact the fitted cluster profiles, but can still elevate the overall χ^2 .

Another potential source of noise worth considering is the primary CMB anisotropies. Bolocam accounts for CMB anisotropies in their noise model by adding astronomical sky realizations based on Keisler et al. (2011) and Reichardt et al. (2012) SPT measurements (Sayers et al. 2013a). In the MUSTANG data, we are not concerned with the primary CMB anisotropies because these are negligible beyond $\ell \gtrsim 6000$ ($\theta \lesssim 2'$) (George et al. 2015). Given the MUSTANG transfer function, we estimate that the expected CMB contamination will fall below $4 \mu\text{Jy}/\text{beam}$, which is well below our noise level, and therefore negligible.

Our pressure profile fits do not change significantly between the chosen Bolocam or X-ray centroids. As seen in Figure 9, MACS 0647 is the only cluster to show significant residuals near the centroid, indicative of a centroid offset. However, given MUSTANG's sensitivity to substructure and potential degeneracy, it is possible that this apparent centroid offset could be due to substructure that is not well separated from the cluster core. We note that the reduced χ^2 (Table 5) indicates that MACS 0647 is still well fit.

3.4.1. Impact of MUSTANG Mean Level on the Pressure Profile

The mean levels in the MUSTANG maps are typically $\lesssim 15 \mu\text{Jy}/\text{beam}$ in amplitude. The subtraction of a mean level within the MUSTANG maps results in a minimal change in the fitted pressure profile shapes, but in every case, it reduces χ^2 (as compared to subtracting no mean level). In the case of MACS 1206, when subtracting a mean level, the parameters γ and C_{500} change by ~ 0.1 , creating a steeper inner pressure profile, where the pressure profile is elevated by $\sim 50\%$ in the innermost $10''$ and elevated by $\sim 5\%$ at $240''$. However, in all other clusters, the changes in the parameters γ and C_{500} are less than 0.05, and corresponding pressure profile changes, between $5''$ and $240''$, are generally less than 5%.

3.4.2. Impact of Potential Substructure on the Pressure Profile

The impact of residual components and point sources is heterogeneous given the varying relevancy of these components. The residual maps and χ^2 suggest that the point-source components are appropriate models for the sources we see in our clusters. MUSTANG maps, removing the fitted point sources, are shown in Figure 3. In Section 4.1, we revisit the impact of point sources on the pressure profile. The residual components generally appear to be sufficient, despite the simplicity of a 2D Gaussian. In the case of MACS 0717, the structure is not well modeled by a 2D Gaussian, but its modeling is minimally impactful because it is sufficiently far from the center. In contrast, if a residual component is not fit in RXJ 1347 and MACS 0744, we find a maximum of 20% and 100% increase in the pressure profile, occurring toward the center (at $4''.5$ radius: MUSTANG's half width at half maximum, HWHM). This increase drops to 3% and 60% at $240''$ (half of Bolocam's FOV). These two clusters exhibit this strong dependence on the treatment of substructure due to the substructures' proximity to the core, where azimuthal averaging does not dilute the signal. In the other clusters, MACS 1206 and MACS 0717, the omission of a residual component

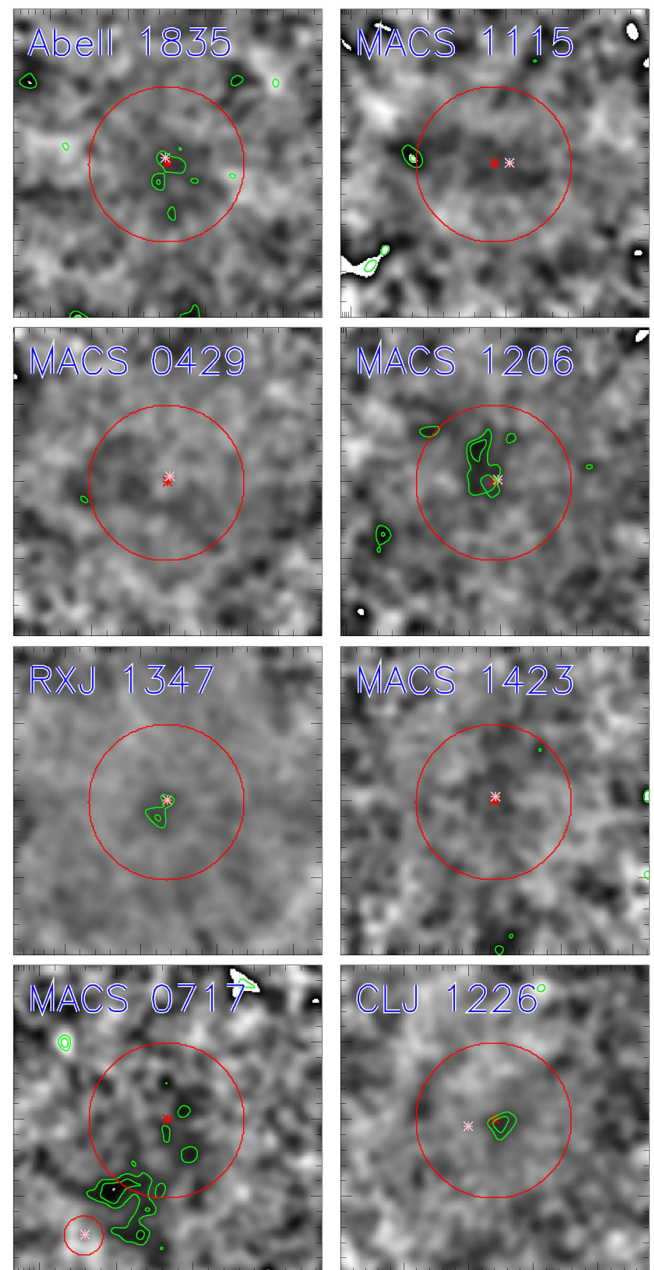


Figure 3. Point source subtracted MUSTANG flux maps for clusters with fitted point sources (Table 3) in MUSTANG data. The color scaling spans the range of $\pm 5 \times \text{Noise}_M$, where Noise_M (for MUSTANG) is given in Table 2. Because Noise_M was calculated in the inner arcminute, the increase in noise with radius is evident with this scaling. The contours are calculated from a signal-to-noise map (i.e., noise-corrected) and start at $\pm 3\sigma$, with 1σ intervals. The red asterisk is the ACCEPT centroid; the pink asterisk is the point-source centroid. All relevant components were fit, but we have subtracted only the point-source model here.

results in a difference in fitted pressure profiles by less than 10%. Residual MUSTANG maps, i.e., maps with all components (including residual components) subtracted, are shown in Figure 9.

4. SZ Pressure Profile Constraints

We have constrained the gNFW parameters P_0 , C_{500} , and γ for 14 individual clusters and present these constraints in Table 5. Given that we find minimal differences between the

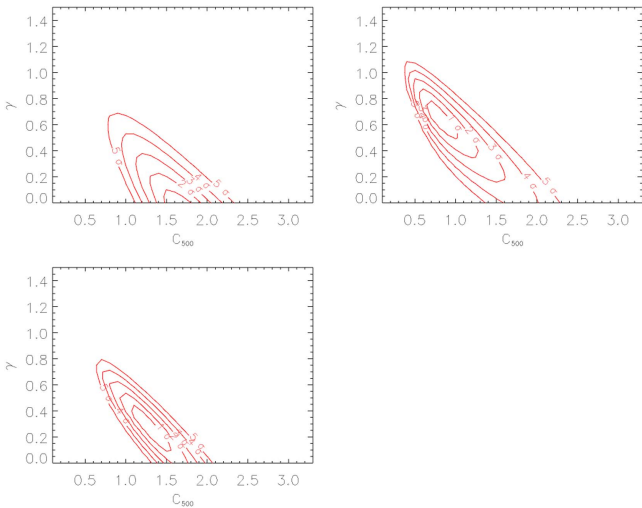


Figure 4. Confidence intervals over all disturbed clusters (upper left panel), cool core clusters (upper right panel), and the entire sample (lower left panel). Cool core clusters include Abell 1835, MACS 1115, MACS 0429, MACS 0329, RXJ 1347, MACS 1311, and MACS 1423. Disturbed clusters include MACS 0329, MACS 1149, MACS 0717, and MACS 0744.

fitted parameters using either the ACCEPT or Bolocam centroids, we report the results using the ACCEPT centroids. We find that 6 of our sample of 14 have best fits of $\gamma = 0$, where we do not allow $\gamma < 0$. We find that our range of C_{500} is sufficient, and that it is generally found to be $0.5 < C_{500} < 2.0$. Across our entire sample, we find the best-fitted gNFW parameters to be $[\gamma, C_{500}, P_0] = [0.3^{+0.1}_{-0.1}, 1.3^{+0.1}_{-0.1}, 8.6^{+2.4}_{-2.4}]$. Cool core clusters show a steeper inner pressure profile, and are fitted with $[\gamma, C_{500}, P_0] = [0.6^{+0.1}_{-0.1}, 0.9^{+0.1}_{-0.1}, 3.6^{+1.5}_{-1.5}]$, and disturbed clusters show a flatter inner pressure profile with fitted parameters: $[\gamma, C_{500}, P_0] = [0.0^{+0.1}_{-0.0}, 1.5^{+0.1}_{-0.2}, 13.8^{+1.6}_{-1.6}]$. These constraints are visualized in Figure 4.

We are further interested in comparing our pressure profile constraints, both individually and as a sample, to previous constraints. To compare to the pressure profiles from ACCEPT2 (Baldi 2014), we fit gNFW profiles to the deprojected pressure profiles of our cluster sample (Section 6.1). We adopt B14 to refer to the ensemble pressure profiles fit to ACCEPT2 data for our sample of 14 clusters. Individually, we find discrepancies in pressure profiles, but as an ensemble there is relatively good agreement. Moreover, the average pressure profile for the 14 clusters has parameter values that are very similar to those found using X-ray data in Arnaud et al. (2010). This can also be seen in Figure 5, where the A10 and B14 pressure profiles are generally consistent with the profile from this work (R16), where deviations are $<30\%$ over $0.03R_{500} < r < R_{500}$ for A10 and $<50\%$ for B14. While all 14 clusters in this work are in Sayers et al. (2013a; hereafter S13), we note that they find a consistently higher average pressure profile. Furthermore, the average pressure profile found by Planck Collaboration et al. (2013; hereafter P13) is higher than our average profile at large radii. In Figure 5, we also include a comparison to the pressure profile determined from simulations in Nagai et al. (2007), denoted as N07. The pressure profiles of N07, A10, and B14 broadly cover the same spatial scales as our work ($0.03R_{500} < r < R_{500}$), while P13 and S13 generally loose sensitivity below $0.1R_{500}$ and are sensitive to scales beyond R_{500} .

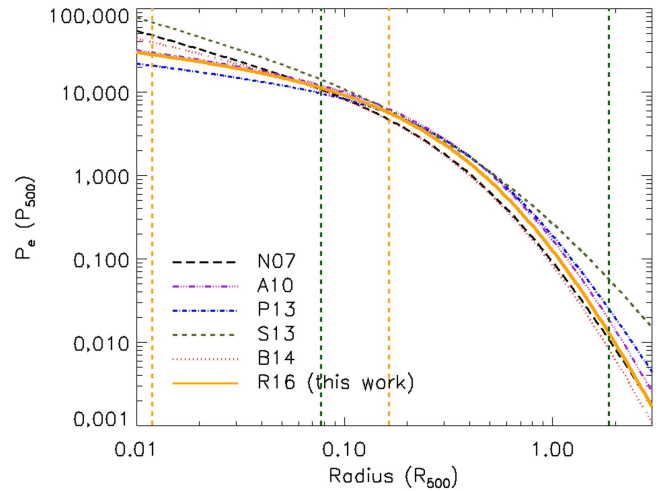


Figure 5. Pressure profiles from this (R16) and other works. We observe that for our 14 clusters, the ACCEPT2 data B14 falls below R16, whereas A10, P13, and S13 show higher pressure at large radii. The pressure profile N07 also agrees well with our work, but shows a steeper inner profile. The dark green dashed lines indicate the extent of Bolocam’s nominal coverage (from HWHM to the radial FOV), and the orange dashed lines indicate the extent of MUSTANG’s nominal coverage.

While our average pressure profiles are in excellent agreement with the previously derived pressure profiles in the region $0.1R_{500} < r < R_{500}$, we see deviations at small and large radii. In Figure 5, we indicate the nominal coverage of each instrument as the minimum HWHM, expressed in R_{500} , and maximum radial FOV, expressed in R_{500} . As demonstrated in Romero et al. (2015), the greatest constraints from individual instruments tends to be at the center (geometric mean) of these two values. It is not too surprising that our fits agree with A10 at large radii, as we have fixed α and β to the A10 values. Despite our 14 clusters being included in the BOXSZ sample (Sayers et al. 2013a), we see that S13 shows higher pressure at all radii. S13, fixing the slope of γ , present a higher pressure at small radii than found here, where the MUSTANG data provide stronger constraints on the pressure gradients in the cluster core and suggest that they are often weaker than previously thought.

We further consider the ratio of individual cluster pressure profiles from our work (P_{SZ}) to the pressure profiles from other works. For comparisons with A10, P13, and S13, we take P_{A10} , P_{P13} , and P_{S13} to be the gNFW profile, which each respective work had fit to their entire sample. For any of these sets (A10, P13, or S13), the ratio P_{SZ}/P_{set} is calculated for each cluster, where only P_{SZ} changes for each cluster. To compare P_{SZ} to ACCEPT2 (P_X), we fit a gNFW profile to ACCEPT2 data (Section 6.1) for each cluster, and thus compare unique P_{SZ} and P_X pressure profiles for each cluster. These ratios are shown in Figure 6, where the shaded regions are influenced both by statistical errors and scatter.

4.1. Fits with $\gamma = 0$

In 6 of our 14 clusters, we find best-fit pressure profiles with $\gamma = 0$, the limit we impose as a prior. There is no clear segregation based on dynamical state or presence of the central point source. Here, we consider two effects that could spuriously bias the cluster central pressures: our choice of centroid and the mis-subtraction of a central point source.

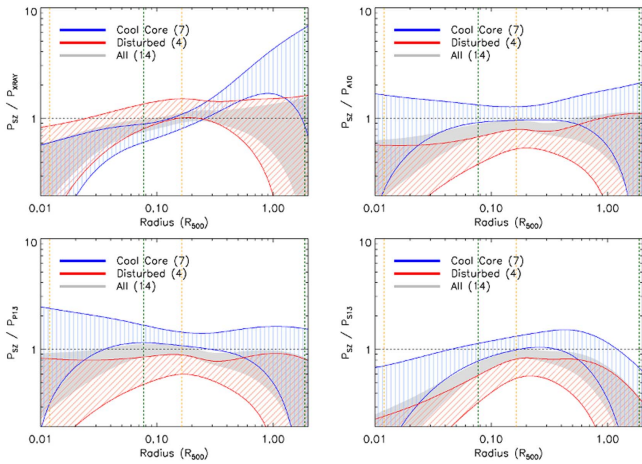


Figure 6. Pressure ratios as compared to different sets, plotted as the central 68% confidence intervals. The ensemble pressure ratios relative to ACCEPT2 (P_x) are calculated per cluster and weighted by the error in the ratio (per radial bin). For the other pressure ratios, the ratio is again calculated per individual cluster, but the comparison pressure profile is the gNFW profile for the entire data set, respectively (i.e., A10, P13, or S13). These ratios are weighted in the same manner. As in Figure 5, the dark green dashed lines indicate the extent of Bolocam’s nominal coverage, and the orange dashed lines indicate the extent of MUSTANG’s nominal coverage.

As it stands, finding slopes in the cores of galaxy clusters that are fit with $\gamma = 0$ is not unprecedented; A10 find 6 of their 31 analyzed clusters in the REXCESS sample have $\gamma = 0$, where all gNFW parameters except β were fit for individual clusters. They find a similar range in C_{500} as we do. They fit for α , which is fit by the range $0.3 < \alpha < 2.5$ over their sample. While A10 is a local ($z < 0.2$) sample, Mantz et al. (2016) find $\gamma = -0.01$, using *Chandra* data, for their sample of 40 galaxy clusters of $0.07 < z < 1.10$. Moreover, in an analysis of X-ray (*Chandra*) data from observations of 80 clusters, McDonald et al. (2014) find $\gamma = 0$ for their low redshift ($0.3 < z < 0.6$), non-cool core clusters, and similarly shallow inner pressure profile slope ($\gamma = 0.05$) for the high-redshift ($0.6 < z < 1.2$) non-cool core clusters. Although these previous studies indicate that $\gamma = 0$ is relatively common, we explore whether systematics related to either our data or analysis methods may produce these results in our fits.

Shallow slopes in the cores of clusters could be suggestive of a centroid offset either between MUSTANG and Bolocam or between SZ and X-ray data. Given the MUSTANG and Bolocam pointing accuracies ($2''$ and $5''$, respectively), it is unlikely that the centroid offsets between MUSTANG and Bolocam are driving the fits to shallow slopes. The difference between SZ (Bolocam) centroids and ACCEPT centroids (Table 1) are large relative to pointing accuracies and thus potentially more important. However, when we adopt Bolocam’s centroid, we find negligible change to the SZ pressure profile as compared to adopting the ACCEPT centroid.

Individually, the Bolocam and MUSTANG data sets yield consistent fits with each other, where changes in best-fit parameters generally occur along the shallow gradient in confidence intervals (i.e., along the degeneracy between C_{500} , and γ).

Additionally, we consider the impact of the assumed flux densities of point sources in the Bolocam maps. There are four clusters (Abell 1835, MACS 0429, RXJ 1347, and MACS 1423) where it was necessary to extrapolate a 140 GHz flux density from lower frequency measurements in order to analyze

the Bolocam data (Sayers et al. 2013a). For point sources other than those in MACS 0429 and RXJ 1347, their uncertainty is less than the noise in the Bolocam maps. Moreover, in all but MACS 0429, the point-source uncertainty is considerably less than the peak Bolocam decrement and mis-estimations of the point-source flux densities in these clusters will not significantly change our results. Therefore, we are left with only MACS 0429, where we believe that the treatment of the point source may affect our results non-trivially.

If we utilize the same low-frequency point-source flux densities in Sayers et al. (2013b) and add in the MUSTANG data, we can recalculate the expected flux densities of point sources at 140 GHz, still assuming one power law. We find that the current Bolocam estimates, with reported uncertainties, are within 1σ of this recalculated value, except for MACS 1423, whose current value falls 1.3σ below the recalculated expectation. This does not address the potential for a break in the power law, which appears to be the case for RXJ 1347.

In RXJ 1347, flux densities of $S_{86} = 4.16 \pm 0.03 \pm 0.25$ mJy and $S_{98} = 3.96 \pm 0.03 \pm 0.24$ mJy have been reported from ALMA (Kitayama et al. 2016) and $S_{86} = 4.9 \pm 0.1$ mJy from CARMA (Plagge et al. 2013). The flux densities reported in Kitayama et al. (2016) come from a baseline cutoff to separate the point source from signal beyond roughly $5''$. Additionally, we note that Adam et al. (2014) used an extrapolated flux of $S_{140} = 4.4 \pm 0.3$, deduced from the power law shown in Pointecouteau et al. (2001), which was calculated from data between 1.4 GHz and 300 GHz.

Only two (MACS 0429 and MACS 1423) of these four clusters are fit by notably low γ values. In addition, for the remaining four clusters in which MUSTANG detects a point source, the Bolocam maps assume no point-source contamination. Of these remaining clusters, only MACS 0717 is fit by a notably low γ , and that is best attributed to the dynamics of the cluster (Appendix B.11).

We also consider that our treatment of point sources in the MUSTANG maps may leave residual emission from point sources, either due to our fitting procedure or the assumption that our assumed point source has a non-trivial extent. Our point-source treatment was designed and extensively tested (e.g., Romero et al. 2015) to accurately remove point sources. In the case of Abell 1835, Romero et al. (2015) find good agreement between the MUSTANG and ALMA (McNamara et al. 2014) point-source flux density.

5. Integrated Compton Y Scaling Relations

We calculate integrated Compton Y values at R_{500} due to the expected minimal scatter at intermediate radii (e.g., Kravtsov & Borgani 2012). We use R_{500} derived from X-ray observations (Mantz et al. 2010), and calculate Y_{sph} , given by

$$Y_{\text{sph}}(R) = \frac{\sigma_T}{m_e c^2} \int_0^R P(r') 4\pi r'^2 dr' \quad (6)$$

and Y_{cyl} , which is given by

$$Y_{\text{cyl}}(R) = \frac{\sigma_T}{m_e c^2} \int_0^R 2\pi r dr \int_r^{R_b} \frac{2r' P(r') dr'}{\sqrt{r'^2 - r^2}}, \quad (7)$$

where we adopt $R_b = 5R_{500}$ as in A10. The error bars on $Y_{\text{sph}}(R_{500})$ and $Y_{\text{cyl}}(R_{500})$ are found by calculating the respective quantities from the pressure profile fits over the 1000 noise realizations, and taking the values encompassing the middle

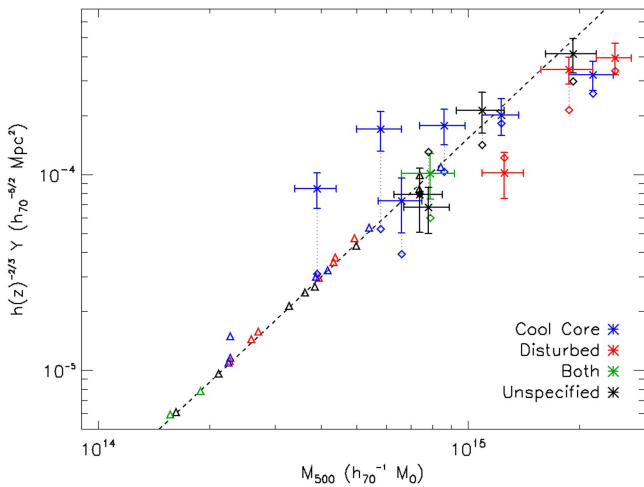


Figure 7. $Y_{\text{sph,SZ}}(R_{500})$ as calculated in this work (Table 5), and M_{500} as calculated from Mantz et al. (2010) are shown as asterisks with error bars. The scaling relation (dashed line) and triangles are from Arnaud et al. (2010) and Pratt et al. (2010). The diamonds are $Y_{\text{sph,X}}(R_{500})$ as calculated from the gNFW fits to the ACCEPT2 pressure profiles. MACS 1311 and MACS 0429 are the notable outliers above the scaling relation.

68%. We take M_{500} from Mantz et al. (2010), who arrive at M_{500} in the following steps: (1) take the measured $f_{\text{gas}}(r_{2500})$ from Allen et al. (2008) and extrapolate it to $f_{\text{gas}}(r_{500})$ by using simulations (2) determine the deprojected gas mass profile from their X-ray data, and (3) combine the deprojected gas mass profile with the value of $f_{\text{gas}}(r_{500})$ to solve for M_{500} (and R_{500}). Mantz et al. (2010) note that the dominant source of systematic uncertainty associated with M_{500} comes from the uncertainty in the assumed $f_{\text{gas}}(r_{2500}) = 0.1104$, which was used in calibrating $f_{\text{gas}}(r_{500}) \approx 0.115$.

We compare our $Y_{\text{sph}}(R_{500}) - M_{500}$ relation to that of A10 in Figure 7. The $Y_{\text{sph}} - M_{500}$ scaling relation calculated in A10 is given as

$$h(z)^{-2/3} Y_{\text{sph}}(xR_{500}) = A_x \left[\frac{M_{500}}{3 \times 10^{14} h_{70}^{-1} M_{\odot}} \right]^{\alpha}, \quad (8)$$

where $\alpha = 1.78$, $A_x = 2.925 \times 10^{-5} I(x) h_{70}^{-1} \text{Mpc}^2$, and $I(1) = 0.6145$. We find 6 of 14 clusters that are more than 2σ in Y_{sph} from the scaling relation. When we consider the mass uncertainty, that number drops to 3. While our sample size is small, the tendency of cool core clusters to lie above the scaling relation and of disturbed clusters to lie below the scaling relation is interesting. Regardless of cluster type, our sample does show a more shallow $Y_{\text{sph},500} - M_{500}$ slope (1.06 ± 0.13) than the predicted self-similar slope (5/3) or 1.78 found in A10. This is consistent with the slope found for the BOXSZ sample by Czakon et al. (2015) for $Y_{\text{cyl},2500} - M_{2500}$ of 1.06 ± 0.12 .

6. Combining SZ and X-Ray Data

The observed SZ and X-ray signal from galaxy clusters differ in their dependence upon the physical properties in the ICM. This difference has, in the past, been exploited to make calculations of the Hubble parameter, H_0 , assuming spherical geometry of galaxy clusters. Alternatively, one could derive the ICM electron temperature without X-ray spectral information, estimate effects such as helium sedimentation, or, relax the

spherical assumption and estimate cluster elongation along the line of sight. Unfortunately, these cannot all be independently constrained. Helium sedimentation will produce a higher P_X relative to P_{SZ} . However, within the predicted range of helium sedimentation (e.g., Peng & Nagai 2009), we lack sufficient sensitivity to constrain it. Thus, we investigate cluster geometry and electron temperature individually, and conclude that differences in the SZ and X-ray spherically derived pressure profiles are unlikely to be explained exclusively by either cluster elongation or ICM temperature distribution.

We compare our SZ data (primarily the pressure profiles) to the ACCEPT2 catalog¹⁶ We correct for the difference in cosmologies assumed in our SZ analysis and that used in ACCEPT2.

6.1. Ellipsoidal Geometry

The geometry of a cluster along the line of sight can be calculated by comparing SZ and X-ray pressure profiles. If we assume azimuthal symmetry in the plane of the sky with scale radius θ_{proj} and a scale radius along the line of sight of θ_{los} , then we denote the elongation/compression along the line of sight with an axis ratio of $c = \theta_{\text{los}}/\theta_{\text{proj}}$, where $c > 1$ implies that the cluster is longer along the line of sight than in the plane of the sky. The X-ray surface brightness is proportional to $\int n_e^2 \Lambda(T, Z) dl \propto \int (P/T)^2 \Lambda(T, Z) dl$, where Z is the abundance of heavy elements and Λ is the X-ray cooling function, while the SZ signal is proportional to $\int P dl$ (Equation (5)). The temperature T can be derived from X-ray. Initially, we will assume that the cluster is spherically symmetric, and derive the pressure profile from the X-ray observations (giving P_X), and from the SZ observations (giving P_{SZ}). If the pressure profiles disagree, one explanation would be the elongation of the cluster along the line of sight. In this case, the elongation is given by

$$c = (P_{\text{SZ}}/P_X)^2. \quad (9)$$

To estimate the ellipticity of clusters, we wish to compare the amplitudes, as fit to X-ray and SZ data, of a given pressure profile shape per cluster. Thus, we fit the ACCEPT2 pressure profiles with a gNFW pressure profile, with α and β fixed at their A10 values: 1.05 and 5.49, respectively. The resultant gNFW profile is then integrated along the line of sight (LOS) to create a Compton y map, and then filtered as discussed in Romero et al. (2015). We refer to this filtered map, per cluster, as the ‘‘ACCEPT2 model’’. Allowing the amplitude to vary, we take P_{SZ} as the amplitude (renormalization) of this ACCEPT2 model when fit to the SZ data, whereby we have effectively set P_X to 1 in Equation (9). Similarly, we define P_B as the fitted amplitude (renormalization) of the ACCEPT2 model to just Bolocam data.

The axis ratio is calculated as $c = P_{\text{SZ}}^2$, and its associated uncertainty is calculated as $\sigma_c^2 = 4P_{\text{SZ}}^4 ((\sigma_{\text{SZ}}/P_{\text{SZ}})_{\text{tot}}^2 + (\sigma_X/P_X)^2)$, where $(\sigma_{\text{SZ}}/P_{\text{SZ}})_{\text{tot}}^2 = (\sigma_{\text{SZ}}/P_{\text{SZ}})_{\text{st.}}^2 + 0.11^2$ includes the total statistical and calibration uncertainties of Bolocam and $(\sigma_X/P_X) = 0.10$ is the calibration uncertainty of ACCEPT2. Table 6 presents relevant fitted gNFW parameters used in calculating the cluster geometry.

¹⁶ ACCEPT2 includes any publicly available *Chandra* observations, thus increasing the sample size and integration times relative to ACCEPT, as reported by Baldi (2014). A public release of ACCEPT2 is anticipated in the near future.

Table 6
ACCEPT2 gNFW Fitted Parameters and Comparison to SZ data

Cluster	P_0	C_{500}	γ	P_{SZ}	k	P_B	c	σ_c	$\Delta P_{SZ,B}/\sigma_{P_{SZ}}$
Abell 1835	10.7	1.4	0.44	0.83 ± 0.03	1.15	0.82 ± 0.03	0.69	0.16	0.48
Abell 611	3.3	0.9	0.62	1.31 ± 0.09	0.92	1.35 ± 0.10	1.71	0.45	0.44
MACS 1115	13.7	1.5	0.35	0.84 ± 0.05	1.14	0.80 ± 0.05	0.70	0.17	0.71
MACS 0429	3.8	1.0	0.71	1.30 ± 0.11	0.64	1.48 ± 0.11	1.70	0.47	1.56
MACS 1206	3.7	1.0	0.49	1.12 ± 0.04	1.01	1.11 ± 0.04	1.24	0.29	-0.03
MACS 0329	4.7	1.2	0.59	1.61 ± 0.09	0.90	1.64 ± 0.09	2.58	0.64	0.41
RXJ 1347	22.8	2.4	0.40	0.95 ± 0.02	1.18	0.94 ± 0.02	0.89	0.20	0.37
MACS 1311	19.2	1.6	0.26	1.28 ± 0.12	0.85	1.40 ± 0.12	1.64	0.47	0.96
MACS 1423	11.2	1.8	0.51	1.26 ± 0.11	0.81	1.39 ± 0.12	1.58	0.44	1.12
MACS 1149	3.3	0.9	0.23	1.24 ± 0.06	0.70	1.28 ± 0.06	1.54	0.37	0.77
MACS 0717	10.2	1.5	0.00	1.36 ± 0.04	0.71	1.39 ± 0.04	1.85	0.43	0.54
MACS 0647	3.6	0.9	0.54	1.29 ± 0.05	1.09	1.27 ± 0.05	1.67	0.40	-0.38
MACS 0744	0.6	0.6	0.93	1.04 ± 0.06	0.94	1.05 ± 0.06	1.08	0.27	0.24
CLJ 1226	20.6	1.3	0.04	0.64 ± 0.04	1.15	0.60 ± 0.04	0.41	0.11	0.97

Note. P_0 , C_{500} , and γ as determined by fitting the ACCEPT2 pressure profiles. P_{SZ} denotes the fitted amplitude (renormalization) of the ACCEPT2 model to the SZ data. P_B denotes the fitted amplitude (renormalization) of the ACCEPT2 model to just Bolocam data. We fix the gNFW parameters $\alpha = 1.05$ and $\beta = 5.49$. The elongation c is the ratio between the scale radius along the line of sight and the projected scale radius (taken to be azimuthally symmetric in the plane of the sky). Positive values in the column $\Delta P_{SZ,B}/\sigma_{P_{SZ}}$ indicate that the core is more spherical than the extended cluster.

Table 7
Normalized Gas Mass Weighted Temperatures

Cluster	$T_{mg,SZ}$	χ^2	DOF	$T_{mg,X}$
Abell 1835	7.29 ± 0.17	29.70	9	7.49
Abell 611	8.56 ± 0.31	2.65	7	6.71
MACS 1115	6.35 ± 0.19	31.55	7	7.04
MACS 0429	3.71 ± 0.25	96.30	5	5.56
MACS 1206	8.44 ± 0.22	31.10	7	10.00
MACS 0329	8.52 ± 0.27	15.67	7	5.64
RXJ 1347	10.73 ± 0.16	14.32	9	9.86
MACS 1311	4.68 ± 0.24	76.77	6	5.18
MACS 1423	6.77 ± 0.27	35.39	6	5.50
MACS 1149	9.04 ± 0.26	30.10	7	7.70
MACS 0717	11.35 ± 0.27	212.62	9	9.06
MACS 0647	10.00 ± 0.28	7.91	6	8.06
MACS 0744	7.30 ± 0.26	5.70	7	6.85
CLJ 1226	8.78 ± 0.39	13.27	4	11.30

Note. The gas mass-weighted temperature proxies, $T_{mg,SZ}$ and $T_{mg,X}$, are calculated by fitting a fixed profile shape, T_{mg} (Equation (11)), to T_{SZ} and T_X . The χ^2 and degrees of freedom for the $T_{mg,SZ}$ fits are tabulated. We find that $T_{mg,SZ}$ is generally larger than $T_{mg,X}$.

This investigation has made the assumption that the geometry of a given cluster is globally consistent. That is, one ellipsoidal geometry applies to all regions of the cluster. However, a cluster should appear more spherical toward the center, where baryons have condensed (e.g., Kravtsov & Borgani 2012, and references therein). Also, the DM and baryonic distributions need not align (one need only look at the Bullet cluster (Markevitch et al. 2004) for a dramatic example). This is not a particular concern to this analysis because we are comparing quantities based on the baryonic distribution, but would be more of a concern when including lensing.

Across our sample, we find an average pressure ratio $\langle P_{SZ} \rangle = 1.14 \pm 0.09$, where we have included the calibration uncertainties in this calculation. We note that the cluster-to-cluster scatter in the pressure ratios is 0.25, which is larger than our uncertainty. That average pressure ratio corresponds to $\langle c \rangle = 1.31 \pm 0.22$, where again, our cluster-to-cluster scatter is

quite large (0.58) compared to our uncertainty. Using cosmological smooth particle hydrodynamics (SPH) simulations, Battaglia et al. (2012) find average 2D (random projection) minor-to-major axis ratios $\simeq 0.95$ based on gas pressure distributions at $\sim R_{500}$ over all cluster masses at $z = 0$. This ratio has some dependence on cluster mass and redshift, where in both cases the deviations from unity grow with increasing mass and with increasing redshift.

Working with a smaller sample than that in Battaglia et al. (2012; 16 clusters) and higher resolution, Lau et al. (2011) use a cosmological simulation with an adaptive mesh refinement (AMR) code to investigate the shape of gas and dark matter, assuming different baryonic physics in two separate runs: a radiative (CSF) and non-radiative (NR) run. While comparable 2D projections of the gas density or pressure are not tabulated in Lau et al. (2011), they find smaller 3D minor-to-major axis ratios of the gas density than in Battaglia et al. (2012). We may conclude that simulations support average elongation values $0.9 < c < 1/0.9$, which is in reasonable agreement with our derived average elongation $\langle c \rangle = 1.31 \pm 0.22$.

Observationally, using SZ and X-ray data on a sample of 25 clusters, De Filippis et al. (2005) find a median projected elongation of 1.24 ± 0.09 , and median elongation along the line of sight (c) of 1.08 ± 0.17 , where two clusters have $c > 2.0$, and three clusters have $1.5 < c < 2.0$. Accounting for our uncertainties, only MACS 0329 and CLJ 1226 are outside (by 1σ) of the range of elongations found in the literature. While this is true, our investigations here are only concerned with elongations along the line of sight, for which we are dominated by clusters with $c > 1$. This could be due to a systematic bias of P_{SZ} high, or P_X low, or even a selection bias within the CLASH sample. The CLASH sample contains X-ray (20) and lensing (5) selected clusters and was not explicitly designed to be orientation unbiased. It is, therefore, not too surprising that we find indications that many of the clusters in our sample are elongated along the line of sight ($c > 1$). Abell 1835 is not in the CLASH sample, but is a notably well-studied cool core cluster, i.e., it is the subject of many studies on the basis of its cool core.

We take the difference, $\Delta P_{SZ,B} = (P_{SZ} - P_B)$ to be indicative that the gas in the core has a different elongation than ICM at moderate to large radii. In particular, for $P_B < 1$, then $P_{SZ} > P_B$ is indicative of a more spherical core and for $P_B > 1$, then a more spherical core will have $P_{SZ} < P_B$. As P_{SZ} and P_B are not independent, we approximate the uncertainty in $\Delta P_{SZ,B}$ as $\sigma_{P_{SZ}}$ and report the pseudo-significances ($\Delta P_{SZ,B}/\sigma_{P_{SZ}}$) of core sphericity (relative to the region outside the center) in Table 5. While none of our determinations individually are above 3σ , it is nonetheless interesting to note the tendency for core sphericity.

6.2. Temperature Profiles

If we assume a given geometry (known ellipticity), then instead of solving for the ellipticity, we can derive a temperature profile, making use of the direct pressure constraints from SZ observations and the electron density constraints from X-ray observations. That is, we calculate

$$T_{SZ} = \frac{P_{SZ}}{n_{e,X}}, \quad (10)$$

where P_{SZ} is the pressure derived from pressure profile fits to the SZ data (Section 4) and $n_{e,X}$ is the deprojected electron density derived from X-ray data by the ACCEPT2 collaboration. For each bin, we assign radial values as the arithmetic mean of its radial bounds. Binned values of P_{SZ} are then calculated from the fitted gNFW profile for each radial value for the corresponding bins used for $n_{e,X}$.

Our SZ and X-ray derived temperature profiles (Figure 8) reveal, on average, larger temperatures than the spectroscopically derived temperatures from ACCEPT2. As an additional means of comparison, we fit an average profile derived in Vikhlinin et al. (2006) for the gas mass weighted temperature:

$$\frac{T(r)}{T_{\text{mg}}} = 1.35 \frac{(x_r/0.045)^{1.9} + 0.45}{(x_r/0.045)^{1.9} + 1} \frac{1}{(1 + (x_r/0.6)^2)^{0.45}}, \quad (11)$$

where $x_r = r/R_{500}$. Thus, since we take R_{500} as known, the shape of the profile is fixed. The values fit to the ACCEPT2 temperatures are reported in Table 1. We fit T_{mg} to our T_{SZ} profiles and T_X profiles from ACCEPT2, which we take as respective gas mass temperature proxies. The results of these fits are reported in Table 7. We compute the ratio $T_{\text{mg,SZ}}/T_{\text{mg,X}}$ of the two fitted gas mass weighted temperature proxies. We find that $\langle T_{\text{mg,SZ}}/T_{\text{mg,X}} \rangle = 1.06$ with an rms scatter of 0.23.

From Figure 8, we see that the shape of T_{mg} is generally quite consistent with the spectroscopic X-ray temperatures, while it is, in some cases, not reflective of the shape of T_{SZ} . Despite the difference in shapes between T_X and T_{SZ} , it is of moderate surprise that the shape of T_{mg} fits similar temperatures between $T_{\text{mg,X}}$ and the $T_{\text{mg,SZ}}$.

In contrast to our results, which indicate, on average, higher values of T_{SZ} than T_X , we note that Rumsey et al. (2016) find the opposite trend when comparing SZ data from the Arcminute Microkelvin Imager (AMI) with *Chandra* X-ray data for a subsample of the CLASH clusters (10 of 25), 7 of which overlap with our sample. However, Rumsey et al. (2016) use a much different technique to constrain T_{SZ} , based solely on the SZ data with strong priors on cluster parameters such as f_{gas} . In addition, the potential systematics in the 15 GHz

interferometric SZ data used by Rumsey et al. (2016) are largely distinct from those related to our higher frequency bolometric SZ images. As a result, it is not possible to make a direct comparison of the results to better ascertain the cause of the discrepancy.

Given the typically long exposure times (our sample has total *Chandra* exposure times, $19.5 < t_{\text{exp}} < 134.1$ ks) required to derive spectroscopic X-ray temperatures, it is likely that deriving temperatures from SZ pressure profiles and X-ray electron densities will be more commonplace as SZ instruments have progressed rapidly in recent years. We consider the how the uncertainties of two temperature derivations ($\sigma_{T_{SZ}}$ and σ_{T_X}) compare within our sample. We find that $\sigma_{T_{SZ}}$ is generally about twice as large as σ_{T_X} . Furthermore, $\sigma_{T_{SZ}}$ is dominated by both the statistical and systematic uncertainties associated with P_{SZ} , where the fractional uncertainties in our SZ pressure profiles are roughly a factor of three larger than the fractional uncertainties in the X-ray electron densities.

Thus far, we have not taken into consideration systematic errors within σ_{T_X} . The systematic errors on T_X are not well quantified, despite evidence that these systematic errors can be notable (e.g., Donahue et al. 2014). We are thus interested in finding for what fractional systematic error do the uncertainties in $\sigma_{T_{SZ}}$ and σ_{T_X} become comparable and find that a systematic uncertainty of 20% on spectroscopic X-ray temperatures results in $\sigma_{T_{SZ}} \sim \sigma_{T_X}$ over our sample.

We should additionally revisit our uncertainties on T_{SZ} to consider the impact of the uncertainty of the cluster geometry on $\sigma_{T_{SZ}}$. With consideration for elongation along the line of sight, $T_{SZ} = (P_{SZ}/n_{e,X})c^{1/2}$, which will result in an additional fractional error term: $(\sigma_c/2c)$ to be added in quadrature. From Battaglia et al. (2012) and Lau et al. (2011), we can likely expect this term to be of the order of 0.1, which is the same as the statistical and systematic uncertainties on P_{SZ} .

6.3. Discussion: Comparison between SZ- and X-Ray-derived Quantities

We find overall agreement in ensemble constraints of the pressure profile between our SZ pressure profiles and those fitted to ACCEPT2 B14 pressure profiles (Figure 5). When calculating elongation along the line of sight, we find an average axis ratio $\langle c \rangle = 1.38 \pm 0.58$. In our temperature analysis, we find the average gas mass weighted temperature ratio $\langle T_{\text{mg,SZ}}/T_{\text{mg,X}} \rangle = 1.06 \pm 0.23$.

While these average values show consistency between the SZ and X-ray quantities, the SZ pressure is, on average, generally larger than the X-ray pressure, especially at larger radii. In our elongation analysis, this pressure difference is manifest as the majority of our clusters showing elongation along the line of sight, which we find is largely consistent with numerical simulations (Section 6.1). Alternatively, in our temperature analysis, we find that T_{SZ} is generally larger than T_X , especially at larger radii. Differences in temperatures could indicate a bias of spectroscopic X-ray temperatures to lower temperatures, as emission will be dominated by the cooler (denser) regions. Moreover, *Chandra* is not sensitive to higher energy photons and therefore constraints on gas hotter than $k_B T \gtrsim 10$ keV are generally poor.

In two clusters, MACS 0717 and CLJ 1226, we attribute the differences in SZ and X-ray pressure profiles to be primarily driven by differences in temperature. The triple merging cluster MACS 0717 (Appendix B.11) does not present a clear shock in

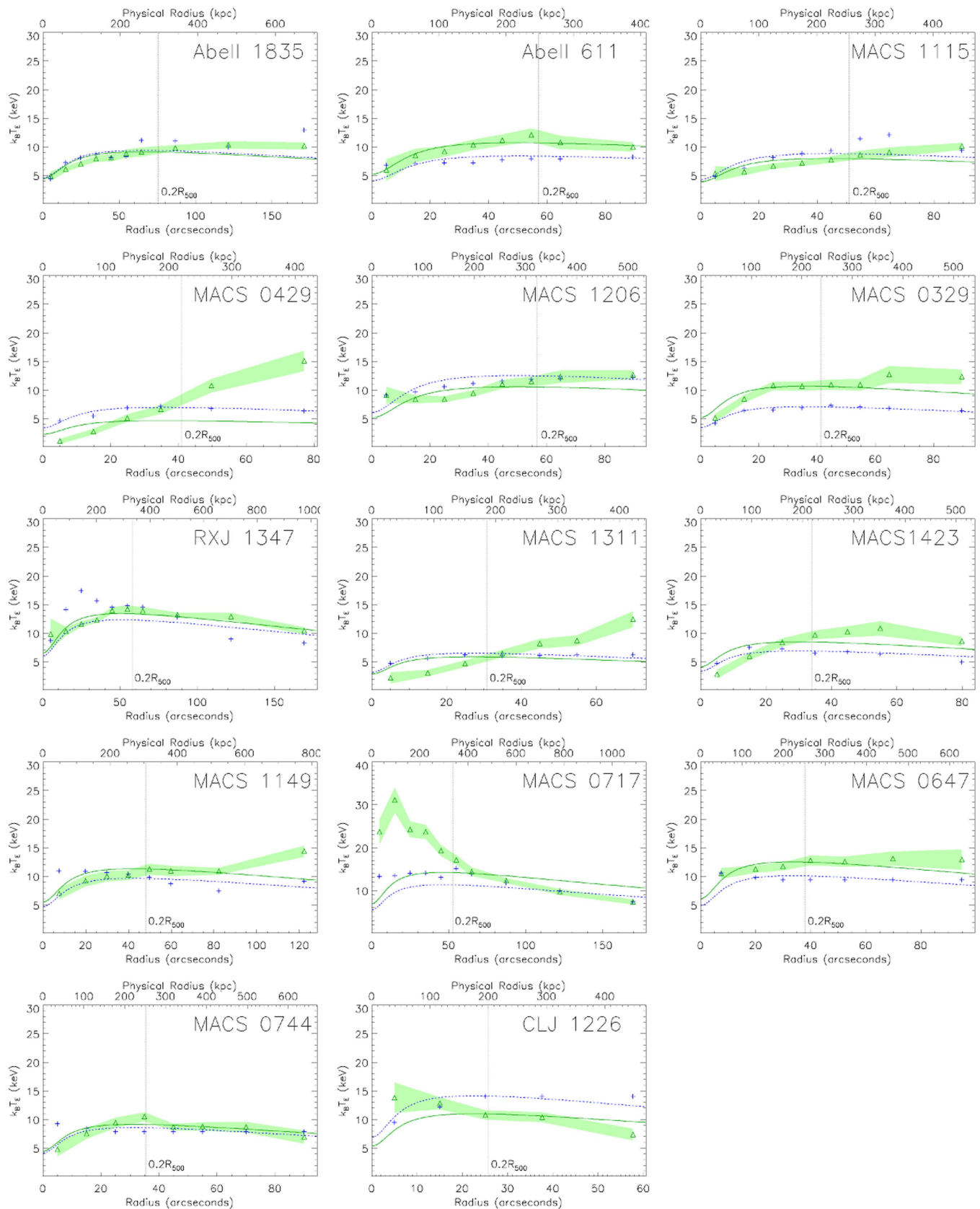


Figure 8. Temperature profiles. The green triangles are derived as $T_{SZ} = P_{SZ}/n_{e,X}$, and the shaded green indicates are 1σ uncertainties, including calibration uncertainties. The blue points are X-ray spectroscopically derived temperatures from ACCEPT2 and associated error bars. The solid green curve is T_{mg} normalized to T_{SZ} , while the dashed blue curve is T_{mg} normalized to T_X .

SZ or X-ray within the central region, but it may be that the merger activity is primarily along the line of sight. The notable enhancement of SZ-to-X-ray spectroscopic temperature in the center is undoubtedly due to merger activity, and bears credence as other studies have found hot (roughly 20 keV in Sayers et al. 2013a; Adam et al. 2016, and 34 keV in Mroczkowski et al. 2012) gas in the region about subcluster C, which would contribute to temperature enhancements at small radii. In CLJ 1226, the average temperature values we derive are not significantly different than those in ACCEPT2, but the slope is reversed. In particular, the ACCEPT2 temperature in CLJ 1226 rises from 10 keV in the core to 15 keV at $r \sim 200$ kpc. In contrast, T_{SZ} shows a more characteristic, declining temperature profile. It is unclear what would cause this difference. We believe that this difference in slope accounts for a non-trivial change in the fitted pressure profile to ACCEPT2 (Section 6.1), which drives the corresponding SZ-fitted normalizations (P_{SZ} and P_B) low.

A third cluster with notable differences in the pressure profiles is MACS 0429. The SZ and X-ray pressure profiles have considerably different shapes. While this may be due, in part, to an increase in temperature with radius, we do not contend that this increase is as dramatic as that shown in Figure 8. It is possible that the intrinsic weakness of the decrement of this cluster, combined with the unusual strength of the central source ($S_{90} = 8$ mJy), has exceeded the capabilities of our point-source treatment (Section 4.1) and could thus be biasing the results on this particular cluster. However, this should primarily affect the inner pressure profile, and Bolocam is constraining the pressure at moderate to large radii to be well above that found in ACCEPT2.

Clumping may also be responsible for raising T_{SZ} relative to T_X at larger radii. Clumping is expected to increase with radius, and thus may account for some of the discrepancy between our inferred temperature and the X-ray spectroscopically derived temperatures. Battaglia et al. (2015) find that clumping is more pronounced for more massive clusters. For the most massive bin of clusters considered, which is most applicable to our sample, the density clumping ($C_{2,\rho} = \langle \rho^2 \rangle / \langle \rho \rangle^2$) at R_{500} is roughly 1.2. Some SZ/X-ray constraints (e.g., Morandi et al. 2013; Morandi & Cui 2014) find clumping factors $C_{2,\rho} \sim 2$ at $R_{200} \sim 1.6R_{500}$, are within agreement with simulations. A clumping factor of 1.2 can account for biasing the T_X low relative to T_{SZ} by roughly $\sim 5\%$.

7. Conclusions

We developed an algorithm to jointly fit gNFW pressure profiles to clusters observed via the SZ effect with MUSTANG and Bolocam. We applied this algorithm to 14 clusters and found that the profiles are consistent with a universal pressure profile found in Arnaud et al. (2010). Specifically, the pressure profile is of the form

$$\tilde{p} = \frac{P_0}{(C_{500}X)^\gamma [1 + (C_{500}X)^\alpha]^{(\beta-\gamma)/\alpha}},$$

where we fixed α and β to values found in Arnaud et al. (2010). A comparison to previous determinations of pressure profiles is shown in Figure 5. Within the radii where we have the greatest constraints ($0.03R_{500} \lesssim r \lesssim R_{500}$), the pressure profile from this work is comparable to the other pressure profiles. This is

further evidenced in the parameters themselves, as seen in Table 5, especially in comparison to A10 parameter values.

With the high resolution of MUSTANG, we were able to identify and remove point sources. MUSTANG is also sensitive to substructure, which we modeled and incorporated in our fitting algorithm. In the MUSTANG maps, we found that substructure in the central regions of clusters is not a rare occurrence, as 4 of our 14 clusters have clearly identified substructure, and 2 more have potential substructure. However, the substructure only impacts the fitted pressure profile above a 10% level for RXJ1347 and MACS 0744, where the substructure (shocks) occurs very near to the core ($\theta \lesssim 20''$).

We find general agreement between the SZ and X-ray pressure profiles for the ensemble of our sample. Additionally, we investigated cluster geometry by taking the ratio between spherically derived pressure profiles as fit to SZ and X-ray data and we found that the clusters have an average axis ratio of $\langle c \rangle = 1.38 \pm 0.58$ (individual axis ratios are tabulated in Table 6). This suggests that most of the clusters in our sample are elongated along the line of sight. This may not be surprising for a heterogeneously selected sample such as CLASH, for which several clusters were chosen for their strong lensing magnifications. We extended our analysis to estimate the relative cluster geometry in the core (from MUSTANG), compared to the larger scale ICM (from Bolocam) and we found some hint that the cores tend to be more spherical than the ICM at larger radii.

When we assumed spherical symmetry and independently calculated temperature, T_{SZ} , from SZ pressure and electron density, we found an average gas mass weighted temperature ratio of $\langle T_{\text{mg,SZ}}/T_{\text{mg,X}} \rangle = 1.06 \pm 0.23$. Furthermore, our profiles of T_{SZ} reveal a trend toward higher temperatures than T_X at larger radii. We argue that higher T_{SZ} temperatures should be expected in clusters where merging activity will heat the gas beyond the sensitivity range of X-ray instruments (for *Chandra*, this is roughly $k_B T \gtrsim 10$ keV).

Cluster geometry appears to play a significant role in yielding different SZ- and X-ray-derived pressure profiles within our sample; however, it is implausible that it is the sole factor to finding larger SZ pressures than X-ray pressures. Other relevant factors include deviations from ellipsoidal geometry; different sensitivities to hot gas in SZ and X-ray observations; and, at large radii, clumping of the ICM.

Finally, as we look forward to the future of galaxy cluster surveys (e.g., SPT3G, ACTpol, WFIRST, SPHEREx, Euclid, LSST, and eRosita), we expect ICM temperature derivations from SZ intensity and X-ray surface brightness (density) to be more common. In our study, the temperatures that we derived in this manner, T_{SZ} , are dominated by uncertainties in the SZ measurements. The fractional uncertainties in our SZ pressure profiles are roughly a factor of three larger than the fractional uncertainties in the X-ray electron densities. Despite this, we find T_{SZ} uncertainties of ~ 2 times larger than the statistical spectroscopic X-ray temperature uncertainties. In light of new SZ instruments (e.g., MUSTANG-2, NIKA2, and ALMA Dicker et al. 2014; Calvo et al. 2016; Kitayama et al. 2016) coming online with vastly improved mapping speeds, our results are encouraging for the prospects of physically characterizing the ICM of newly discovered systems with rapid follow-up programs.

While at NRAO and UVA, support for C.R. was provided through the Grote Reber Fellowship administered by AUI/NRAO. Support for C.R., P.K., and A.Y. was provided by the Student Observing Support (SOS) program. Support for T.M. was partially provided by the National Research Council Research Associateship Award at the U.S. Naval Research Laboratory. Basic research in radio astronomy at NRL is supported by 6.1 Base funding. J.S. was partially supported by a Norris Foundation CCAT Postdoctoral Fellowship and by NSF/AST-1313447.

The National Radio Astronomy Observatory is a facility of the National Science Foundation, which is operated under cooperative agreement with Associated Universities, Inc. The GBT observations used in this paper were taken under NRAO proposal IDs GBT/08A-056, GBT/09A-052, GBT/09C-020, GBT/09C-035, GBT/09C-059, GBT/10A-056, GBT/10C-017, GBT/10C-026, GBT/10C-031, GBT/10C-042, GBT/11A-001, and GBT/11B-009 and VLA/12A-340. We thank the GBT operators Dave Curry, Greg Monk, Dave Rose, Barry Sharp, and Donna Stricklin for their assistance.

The Bolocam observations presented here were obtained from the Caltech Submillimeter Observatory, which, when the data used in this analysis were taken, was operated by the California Institute of Technology under cooperative agreement with the National Science Foundation. Bolocam was constructed and commissioned using funds from NSF/AST-9618798, NSF/AST-0098737, NSF/AST-9980846, NSF/AST-0229008, and NSF/AST-0206158. Bolocam observations were partially supported by the Gordon and Betty Moore Foundation, the Jet Propulsion Laboratory Research and Technology Development Program, as well as the National Science Council of Taiwan grant NSC100-2112-M-001-008-MY3.

Access to ACCEPT2 data was possible due to the gracious assistance of Rachael Salmon. We thank the anonymous referee for helpful comments.

Appendix A Residual Maps

In Figure 9 we present residual maps of MUSTANG data, where all relevant model components (see Section 3.2) have been fit and subtracted.

Appendix B Notes on Individual Clusters

Below, we provide notes on individual clusters in our sample, focusing primarily on previous SZ, X-ray, and lensing studies.

B.1. Abell 1835 ($z = 0.25$)

Abell 1835 is a well-studied massive cool core cluster. The cool core was noted to have substructure in the central $10''$ by Schmidt et al. (2001) and identified as being due the central AGN by McNamara et al. (2006). Abell 1835 has also been extensively studied via the SZ effect (Reese et al. 2002; Benson et al. 2004; Bonamente et al. 2006; Sayers et al. 2011; Mauskopf et al. 2012). The models adopted were either beta models or generalized beta models, and tend to suggest a shallow slope for the pressure interior to $10''$. Previous analysis of Abell 1835 with MUSTANG data (Korngut et al. 2011) detected the SZ effect decrement, but not at high significance, which is consistent with a featureless, smooth, broad signal.

Our updated MUSTANG reduction of Abell 1835, shown in Figure 1, has the same features as in Korngut et al. (2011).

B.2. Abell 611 ($z = 0.29$)

The MUSTANG map (Figure 1) shows an enhancement south of the X-ray centroid, and the Bolocam map shows elongation toward the south–southwest. Weak lensing maps are suggestive of a southwest–northeast elongation (Newman et al. 2009; Zitrin et al. 2015). Using the density of galaxies, Lemze et al. (2013) find a core and a halo that align with the elongation seen in the SZ. We note that AMI (AMI Consortium et al. 2012) and De Filippis et al. (2005) also see an elongation in the same direction in the plane of the sky. However, more recent AMI observations (Rumsey et al. 2016) show almost no elongation. Along the line of sight, De Filippis et al. (2005) calculate an elongation $c = 1.05 \pm 0.37$. Despite these notions of elongation, within the sample investigated in AMI Consortium et al. (2012), Abell 611 is the most relaxed cluster in their sample and that the X-ray data presented from LaRoque et al. (2006) is very circular and uniform. Despite being relaxed, Abell 611 is not listed as a cool core cluster (nor disturbed; Sayers et al. 2013a).

In an analysis of the dark matter distribution, Newman et al. (2009) find that the core (logarithmic) slope of the cluster is shallower than an NFW model, with $\beta_{\text{DM}} = 0.3$, where the dark matter distribution has been characterized by yet another generalization of the NFW profile:

$$\rho(r) = \frac{\rho_0}{(r/r_s)^{\beta_{\text{tot}}}(1+r/r_s)^{3-\beta_{\text{tot}}}}. \quad (12)$$

They find the distribution of dark matter within Abell 611 to be inconsistent with a single NFW model.

B.3. MACS 1115 ($z = 0.36$)

MACS 1115 is listed as a cool core cluster (Sayers et al. 2013a). It is among seven CLASH clusters that show unambiguous ultraviolet (UV) excesses attributed to unabsorbed star formation rates of $5\text{--}80 M_{\odot} \text{ yr}^{-1}$ (Donahue et al. 2015). MUSTANG detects a point source in MACS 1115, which is coincident with its BCG. MACS 1115 is fit by a fairly steep inner pressure profile slope to the SZ data (Table 5). Adopting the Bolocam centroid, the inner pressure profile slope is notably reduced, yet the goodness of fit is not significantly changed. In particular, the Bolocam image shows a north–south elongation (particularly to the north of the centroids). In contrast, weak and strong lensing (Zitrin et al. 2015) show a more southeast–northwest elongation.

B.4. MACS 0429 ($z = 0.40$)

MACS 0429 has been well studied in the X-ray (Comerford & Natarajan 2007; Schmidt & Allen 2007; Allen et al. 2008; Maughan et al. 2008; Mann & Ebeling 2012) MACS 0429 is identified as a cool core cluster (cf. Mann & Ebeling 2012; Sayers et al. 2013a). The bright point source in the MUSTANG image is the cluster BCG, which is noted as having an excesses UV emission (Donahue et al. 2015). Of the point sources observed by MUSTANG, this has the shallowest spectral index between 90 GHz and 140 GHz of $\alpha_{\nu} = 0.55$.

Despite MACS 0429's stature as a cool core cluster, its pressure profile (Table 5) is surprisingly shallow in the core, and shows elevated pressure relative to X-ray derived pressure

at moderate radii. The offset between the Bolocam centroid (Sayers et al. 2013a) and ACCEPT (Cavagnolo et al. 2009) centroid is 100 kpc, which is notably larger than the X-ray-optical separations of the cluster peaks and centroids reported in Mann & Ebeling (2012) of 12.8 and 19.5 kpc respectively. Siegel et al. (2016) report an excess in SZ pressure (Bolocam) relative to X-ray (*Chandra*) pressure at moderate to large radii.

B.5. MACS 1206 ($z = 0.44$)

MACS 1206 has been observed extensively (e.g., Ebeling et al. 2001, 2009; Gilmour et al. 2009; Umetsu et al. 2012; Zitrin et al. 2012b; Biviano et al. 2013; Sayers et al. 2013a). It is not categorized as a cool core or a disturbed cluster (Sayers et al. 2013a). Using weak lensing data from Subaru, Umetsu et al. (2012) find that the major–minor axis ratio of projected mass is $\gtrsim 1.7$ at 1σ . They infer that this high ellipticity and alignment with the BCG, optical, X-ray, and LSS shapes are suggestive that the major axis is aligned close to the plane of the sky. In Young et al. (2015), substructure is identified that corresponds to an optically identified subcluster, which may either be a merging subcluster or a foreground cluster. In this analysis, the SZ signal observed by MUSTANG is well modeled by a residual component (coincident with the subcluster) and a spherical bulk ICM component. We note that the Bolocam contours of MACS 1206 do not exhibit much ellipticity. We do find that MACS 1206 has a major–minor axis ratio of 1.24 ± 0.29 (Table 6), where the major axis is along the line of sight.

B.6. MACS 0329 ($z = 0.45$)

MACS 0329 has the distinction of being listed as both a cool core and disturbed cluster. Although it has been classified as relaxed (Schmidt & Allen 2007), substructure has been noted (Maughan et al. 2008), and it earns its cool core and disturbed classifications based on central weighting of X-ray luminosity and comparing centroid offsets between optical and X-ray data (Sayers et al. 2013a). The elongation of the weak lensing and strong lensing are toward the northwest and southeast of the centroid.

MACS 0329 has two systems with multiple images: one at $z = 6.18$ and the other at $z = 2.17$. The Einstein radii for these two systems are $r_E = 34''$ and $r_E = 28''$, respectively (Zitrin et al. 2012a), which is noted as being typical for relaxed, well-concentrated lensing clusters.

B.7. RXJ1347 ($z = 0.45$)

RXJ1347 is one of the most luminous X-ray clusters, and has been well studied in radio, SZ, lensing, optical spectroscopy, and X-rays (e.g., Schindler et al. 1995; Pointecouteau et al. 1999; Komatsu et al. 2001; Allen et al. 2002; Kitayama et al. 2004; Gitti et al. 2007a; Bradač et al. 2008; Miranda et al. 2008; Ota et al. 2008). X-ray contours have long suggested that RXJ1347 is a relaxed system (e.g., Schindler et al. 1997), and it is classified as a cool core cluster (e.g., Mann & Ebeling 2012; Sayers et al. 2013a).

Indeed, the first sub-arcminute SZ observations (Komatsu et al. 2001; Kitayama et al. 2004) saw an enhancement to the southeast of the cluster X-ray peak, which was suggested as being due to shock heating. This enhancement was confirmed by MUSTANG (Mason et al. 2010). Further measurements were made with CARMA (Plagge et al. 2013), which find

that 9% of the thermal energy in the cluster is in sub-arcminute substructure. Most recently, Kitayama et al. (2016) has observed this cluster with ALMA to a resolution of $5''$. At low radio frequencies (Ferrari et al. 2011, 237 MHz and 614 MHz), Gitti et al. (2007b, 1.4 GHz) find evidence for a radio mini-halo in the core of RXJ1347. The cosmic-ray electrons are thought to be reaccelerated because of the shock and sloshing in the cluster (Ferrari et al. 2011).

We observe a point source (coincident with the BCG) with a flux density of 7.40 ± 0.58 mJy. A previous analysis of the MUSTANG data found the point-source flux density to be 5 mJy (Mason et al. 2010). The difference in the flux densities is likely accounted for by the different fitting approaches, primarily that (1) we filter the beam shape (a double Gaussian), (2) we simultaneously fit the components, and (3) we assume a steeper profile in the core than the beta model assumed in Mason et al. (2010). Lower frequency radio observations found the flux density of the source to be 10.81 ± 0.19 mJy at 28.5 GHz (Reese et al. 2002), and 47.6 ± 1.9 mJy at 1.4 GHz (Condon et al. 1998). The BCG is observed to have a UV excess (Donahue et al. 2015).

Despite the classification of being a cool core cluster, it is also observed that there are hot regions, initially constrained as $k_B T > 10$ keV (e.g., Allen et al. 2002; Bradač et al. 2008), and more recently constrained to even hotter temperatures ($k_B T > 20$ keV Johnson et al. 2012), indicative of an unrelaxed cluster. Johnson et al. (2012) also interpret the two cold fronts as being due to sloshing, where a subcluster has returned for a second passage.

Several previous studies have found similar evidence for compression along the line of sight in this cluster (e.g., Plagge et al. 2013, and references therein). However, the compression we find in this study is less severe as in Plagge et al. (2013).

B.8. MACS 1311 ($z = 0.49$)

MACS 1311 is listed as a cool core cluster (e.g., Sayers et al. 2013a), and appears to have quite circular contours in the X-ray and lensing images, yet has evidence for some disturbance, given its classification in Mann & Ebeling (2012). However, the SZ contours from Bolocam show some enhancement to the west, and has a notable centroid shift ($27''7$, 167 kpc) westward from the X-ray centroid. When fitting pressure profiles to this cluster, it appears that the enhanced SZ pressure at moderate radii ($r \sim 100''$) is due to this enhancement, especially when noting that we use the X-ray centroid. Adopting the Bolocam centroid does not change the pressure profile much, and we still observe a pressure enhancement at moderate radii. In contrast, in their analysis, Siegel et al. (2016) find that X-ray (*Chandra*) and SZ (Bolocam) data are in good agreement with a spherical ICM model, which is supported primarily with thermal pressure.

B.9. MACS 1423 ($z = 0.54$)

MACS 1423 is a cool core cluster (Mann & Ebeling 2012; Sayers et al. 2013a). While the Bolocam contours are quite concentric and suggestive of a relaxed cluster, the centroid is still offset from the X-ray peak by an appreciable angle ($19''8$, 126 kpc). While AMI (Rumsey et al. 2016) shows a perturbation/extension to the southwest of the cluster, their analysis is supportive of MACS 1423 being a relaxed cluster. Similar to MACS 1311, the pressure is slightly less than the

ACCEPT2 X-ray derived pressure in the core and slightly greater at moderate radii. While this is expected for a centroid offset, we find that adopting the Bolocam centroid again yields no substantial difference in the SZ pressure profile. Both our analysis and that of Siegel et al. (2016) find good agreement between SZ and X-ray pressure profiles. We observe a point source (the cluster BCG) with a flux density of 1.36 ± 0.13 mJy, which is also observed to have a UV excess (Donahue et al. 2015).

B.10. MACS 1149 ($z = 0.54$)

MACS 1149 is classified as a disturbed cluster (e.g., Mann & Ebeling 2012; Sayers et al. 2013a), and lensing studies have found that a single DM halo does not describe the cluster well, but rather at least four large-scale DM halos are used to describe the cluster (Smith et al. 2009). A large radial velocity dispersion (1800 km s^{-1} Ebeling et al. 2007) is observed, indicative of merger activity along the line of sight. X-ray, SZ, and lensing (particularly strong lensing) all show elongation in the northwest–southeast direction. More recently, Golovich et al. (2016) investigate the dynamics of the cluster, identifying three subclusters, with merger activity (velocities) primarily in the plane of the sky. SZ data from AMI (Rumsey et al. 2016) does not strongly indicate merger activity, arguably because the mass of the primary halo is much greater than the subhalos. Morphologically, the SZ map from AMI does show minor asphericity.

While the Bolocam map of this cluster shows a modest elongation in the northwest–southeast direction, it is well modeled as a spherical cluster. Our SZ derived pressure profile roughly matches the shape of the X-ray derived pressure profile, with the SZ pressure consistently greater than the X-ray pressure. We calculate that the axis along the line of sight is 1.54 ± 0.37 (Section 6.1) times greater than the axes in the plane of the sky. In the MUSTANG map, we see a 3σ feature to the east of the centroids, but it is not clear that this is associated with any particular feature.

B.11. MACS 0717 ($z = 0.55$)

Despite MACS 1149’s impressive merging activity, MACS 0717 is thought to be the most disturbed massive cluster at $z > 0.5$ (Ebeling et al. 2007), which appears to be accreting matter along a 6-Mpc-long filament (Ebeling et al. 2004), and has the largest known Einstein radius ($\theta_e \sim 55''$; Zitrin et al. 2009). Four distinct components are identified from X-ray and optical analyses (Ma et al. 2009), and the lensing analyses (Zitrin et al. 2009; Limousin et al. 2012) find agreement in the location of these four mass peaks with those from the X-ray and optical. While the complex X-ray morphology is not evident in AMI (Rumsey et al. 2016) or Bolocam SZ maps, there is still asphericity in the maps.

There are four identified subclusters (labeled A through D Ma et al. 2009). They find that subcluster C is the most massive component, while subcluster A is the least massive, and subclusters B and D are likely remnant cores. The velocities of the components from spectroscopy are found to be $(v_A, v_B, v_C, v_D) = (+278_{-339}^{+295}, +3238_{-242}^{+252}, -733_{-478}^{+486}, +831_{-800}^{+843}) \text{ km s}^{-1}$ (Ma et al. 2009). The first indication of detection of the kSZ signal toward these subclusters was presented in Mroczkowski et al. (2012), with a subsequent paper from Sayers et al. (2013a) having the first significant detection and derived cluster

velocities. Most recently, Adam et al. (2016) has mapped the kSZ signal and derived model-dependent subcluster velocities.

MACS 0717 has also been observed at 610 MHz with the Giant Metrewave Radio Telescope (GMRT), which reveals both a radio halo and a radio relic (van Weeren et al. 2009). This is interpreted as likely being due to a diffuse shock acceleration (DSA). More recently, however, deep, higher resolution JVLA data have found a connection between a central radio source and the diffuse emission, and favor re-acceleration as the source of the relativistic electrons (van Weeren et al. 2017).

We observe a foreground radio galaxy, well outside the cluster centered, which we model as a point source here, with a flux density of 2.08 ± 0.25 mJy at 90 GHz. This was previously reported with an integrated flux density of 2.8 ± 0.2 mJy and an extended shape of $14.''4 \times 16.''1$ (Mroczkowski et al. 2012). However, improved beam modeling has allowed us to model the foreground galaxy given a known beam shape. It is also worth noting that the MUSTANG data itself has been processed slightly differently from that presented in Mroczkowski et al. (2012); in this work, the map is produced with a common calculated as the mean across detectors, whereas, in Mroczkowski et al. (2012), the common mode was calculated as the median across detectors.

B.12. MACS 0647 ($z = 0.59$)

MACS 0647 is at $z = 0.591$ and is classified as neither a cool core nor a disturbed cluster (Sayers et al. 2013a). It was included in the CLASH sample due to its strong lensing properties (Postman et al. 2012). Gravitational lensing (Zitrin et al. 2011), X-ray surface brightness (Mann & Ebeling 2012), and SZ effect (MUSTANG, see Figure 1, and Bolocam) maps all show elongation in an east–west direction. Rumsey et al. (2016) find a circular SZ morphology with AMI, and take the discrepancies in the SZ and X-ray temperatures as an indication of a recent head-on merger. In the joint analysis presented here, we see that the spherical model provides an adequate fit to both data sets, as evidenced in Table 5. Still, from Figure 9, it appears that some elongation of the bulk ICM or residual feature would better describe the cluster center.

B.13. MACS 0744 ($z = 0.70$)

MACS 0744 is neither classified as a cool core cluster nor a disturbed cluster (Mann & Ebeling 2012; Sayers et al. 2013a), but qualifies as a relaxed cluster (Mann & Ebeling 2012). There is a dense X-ray core, and a doubly peaked red sequence of galaxies, as found by Kartaltepe et al. (2008). The gas is also found to be rather hot: $k_B T = 17.9_{-3.4}^{+10.8}$ keV, as determined by combining SZ and X-ray data (LaRoque et al. 2003). AMI observations (Rumsey et al. 2016) show some elongation in the plane of the sky in their SZ map of this cluster, but they otherwise find that the cluster is in a relaxed state.

The data presented here is the same as in Korngut et al. (2011), but has been processed differently: again, the primary difference is in the treatment of the common mode. Additionally, Korngut et al. (2011) optimize over the low-pass filtering of the common mode and do not implement a correction factor for the SNR map. The surface brightness significance of the shock feature is the same, but is perhaps less bowed than the kidney bean shape seen previously. The excess found in Korngut et al. (2011) marked the first clear detection

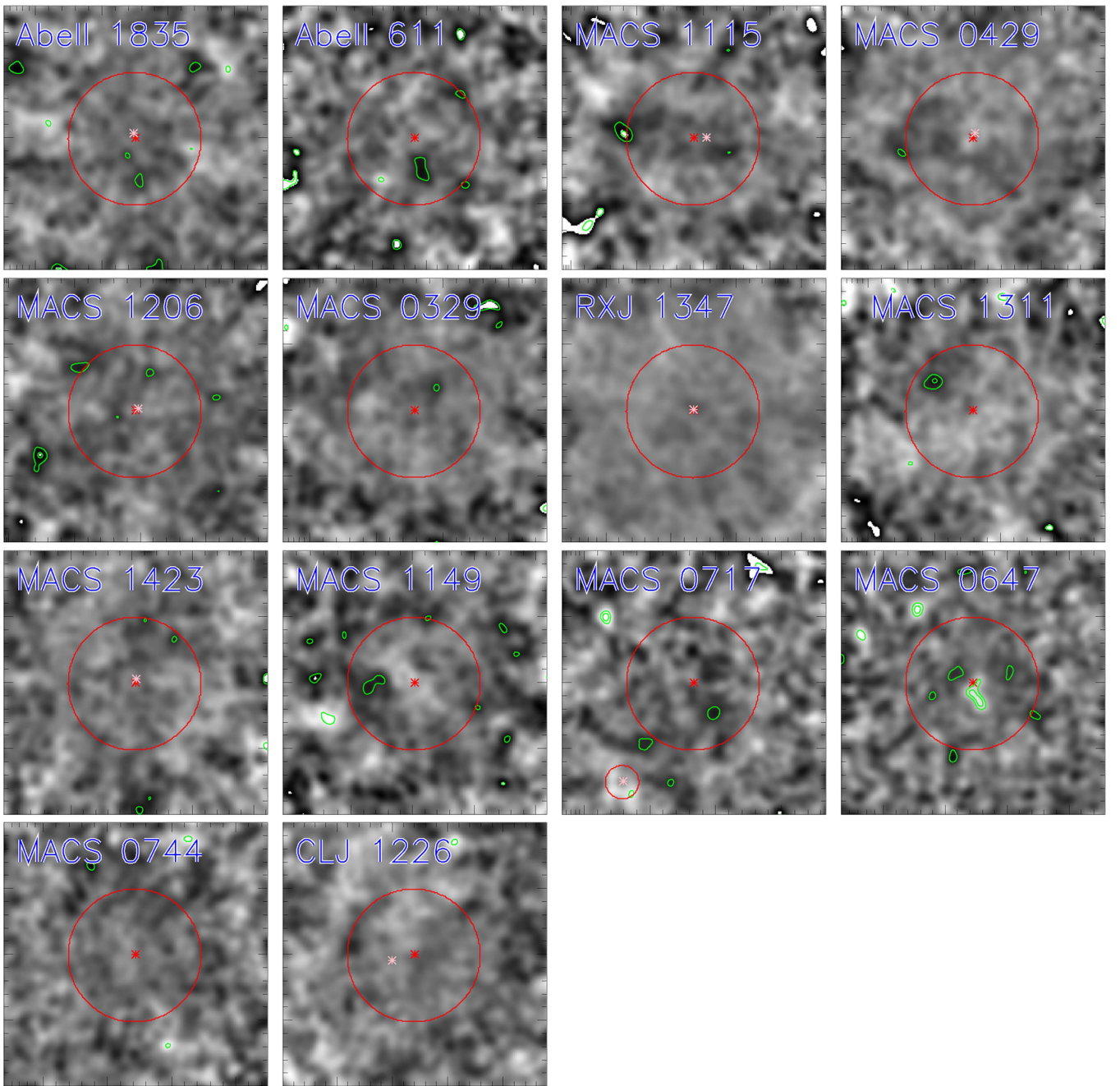


Figure 9. Residual MUSTANG flux maps of all clusters. The color scaling spans the range of $\pm 5 \times \text{Noise}_M$, where Noise_M (for MUSTANG) is given in Table 2. Because Noise_M was calculated in the inner arcminute, the increase in noise with radius is evident with this scaling. The contours are calculated from a signal-to-noise map (i.e., noise-corrected) and start at $\pm 3\sigma$, with 1σ intervals. The red asterisk is the ACCEPT centroid; the pink asterisk is the point-source centroid (if a point source was subtracted). All relevant components, including any residual component, were fit and subtracted.

of a shock in the SZ that had not been previously been known from X-ray observations. Korngut et al. (2011) reanalyze the X-ray data with the knowledge of the shocked region from MUSTANG, and calculate the Mach number of the shock based on (1) the shock density jump, (2) stagnation condition between the pressures at the edge of the cold front and just ahead of the shock, and (3) temperature jump across the shock, and find Mach numbers between 1.2 and 2.1, with a velocity of 1827^{+267}_{-195} km s⁻¹. The shocked region (region II in Korngut et al. 2011) is well modeled with 19.7 keV gas.

B.14. CLJ 1226 ($z = 0.89$)

CLJ 1226 is a well-studied high-redshift cluster (e.g., Mroczkowski et al. 2009; Bulbul et al. 2010; Adam et al. 2015). Adam et al. (2015) find a point source at R.A. 12:27:00.01 and decl. +33:32:42 with a flux density of 6.8 ± 0.7 (stat.) ± 1.0 (cal.) mJy at 260 GHz and 1.9 ± 0.2 (stat.) at 150 GHz. This is not the same point source seen in Korngut et al. (2011), which is reported as a point source with 4.6σ significance in surface brightness, and can be fit in our current analysis as a point source with a flux density of

0.33 ± 0.13 mJy. A short VLA filler observation (VLA-12A-340, D-array, at 7 GHz) was performed to follow-up this potential source. To a limit of $\sim 50 \mu\text{Jy}$ nothing is seen, other than the clearly spatially distinct radio source associated with the BCG at the cluster center (1 mJy at 7 GHz and 3.2 mJy in NVSS). Rumsey et al. (2016) find a point source of weak significance with a flux density of ~ 0.18 mJy in CLJ 1226 (at 15 GHz); however, coordinates are not provided and the location indicated on the maps would be consistent with either the point source found by Adam et al. (2015) or Korngut et al. (2011). In contrast, the point source found in Adam et al. (2015) is fit to our data with a flux density of 0.36 ± 0.11 mJy. Given the slight increase in significance of the point source from Adam et al. (2015), we adopt that point-source location for our pressure profile analysis of CLJ 1226.

In the previous analysis of the MUSTANG data, Korngut et al. (2011) find a ridge of significant substructure after subtracting a bulk SZ profile (N07, fitted to SZA data). They find that this ridge, southwest of the cluster center, alongside X-ray profiles, are consistent with a merger scenario. Rumsey et al. (2016) also take the discrepancy that they find between SZ and X-ray temperature as indicative a merger scenario. When comparing to merger simulations, they find CLJ 1226 could be consistent with a head-on minor merger. Adam et al. (2015) found evidence for a disturbed core, but relaxed on large scales. However, in this work, we do not find any significant substructure after fitting a bulk component, or other indication of merger activity.

Appendix C Data Products

We have made MUSTANG data products for the sample of clusters analyzed in this paper available at: https://safe.nrao.edu/wiki/bin/view/GB/Pennarray/MUSTANG_CLASH. Links to accompanying Bolocam and ACCEPT data are available from this website as well. In particular, we have publicized the final data maps, noise maps, and signal-to-noise (SNR) maps used in this analysis, as well as transfer functions for individual clusters. Further documentation is available on the website.

References

- Abramopoulos, F., Chanan, G. A., & Ku, W. H.-M. 1981, *ApJ*, 248, 429
 Adam, R., Bartalucci, I., Pratt, G. W., et al. 2016, arXiv:1606.07721
 Adam, R., Comis, B., Macías-Pérez, J. F., et al. 2014, *A&A*, 569, A66
 Adam, R., Comis, B., Macías-Pérez, J. F., et al. 2015, *A&A*, 576, A12
 Allen, S. W., Rapetti, D. A., Schmidt, R. W., et al. 2008, *MNRAS*, 383, 879
 Allen, S. W., Schmidt, R. W., & Fabian, A. C. 2002, *MNRAS*, 335, 256
 AMI Consortium, Hurley-Walker, N., Bridle, S., et al. 2012, *MNRAS*, 419, 2921
 Arnaud, M., Pratt, G. W., Piffaretti, R., et al. 2010, *A&A*, 517, A92
 Baldi, A. 2014, in 15 Years of Science with Chandra, Posters from the Chandra Science Symp., P8
 Battaglia, N., Bond, J. R., Pfrommer, C., & Sievers, J. L. 2012, *ApJ*, 758, 75
 Battaglia, N., Bond, J. R., Pfrommer, C., & Sievers, J. L. 2015, *ApJ*, 806, 43
 Benson, B. A., Church, S. E., Ade, P. A. R., et al. 2004, *ApJ*, 617, 829
 Biviano, A., Rosati, P., Balestra, I., et al. 2013, *A&A*, 558, A1
 Bonamente, M., Hasler, N., Bulbul, E., et al. 2012, *NJPh*, 14, 025010
 Bonamente, M., Joy, M. K., LaRoque, S. J., et al. 2006, *ApJ*, 647, 25
 Borgani, S., Murante, G., Springel, V., et al. 2004, *MNRAS*, 348, 1078
 Bradač, M., Schrabback, T., Erben, T., et al. 2008, *ApJ*, 681, 187
 Bulbul, G. E., Hasler, N., Bonamente, M., & Joy, M. 2010, *ApJ*, 720, 1038
 Calvo, M., Benoît, A., Catalano, A., et al. 2016, *JLTP*, 184, 816
 Cavagnolo, K. W., Donahue, M., Voit, G. M., & Sun, M. 2008, *ApJ*, 682, 821
 Cavagnolo, K. W., Donahue, M., Voit, G. M., & Sun, M. 2009, *ApJS*, 182, 12
 Comerford, J. M., & Natarajan, P. 2007, *MNRAS*, 379, 190
 Condon, J. J., Cotton, W. D., Greisen, E. W., et al. 1998, *AJ*, 115, 1693
 Crawford, C. S., Allen, S. W., Ebeling, H., Edge, A. C., & Fabian, A. C. 1999, *MNRAS*, 306, 857
 Czakon, N. G., Sayers, J., Mantz, A., et al. 2015, *ApJ*, 806, 18
 De Filippis, E., Sereno, M., Bautz, M. W., & Longo, G. 2005, *ApJ*, 625, 108
 Dicker, S. R., Ade, P. A. R., Aguirre, J., et al. 2014, Proc. SPIE, 9153, 0
 Dicker, S. R., Korngut, P. M., Mason, B. S., et al. 2008, Proc. SPIE, 7020, 05
 Donahue, M., Connor, T., Fogarty, K., et al. 2015, *ApJ*, 805, 177
 Donahue, M., Voit, G. M., Mahdavi, A., et al. 2014, *ApJ*, 794, 136
 Ebeling, H., Barrett, E., & Donovan, D. 2004, *ApJL*, 609, L49
 Ebeling, H., Barrett, E., Donovan, D., et al. 2007, *ApJL*, 661, L33
 Ebeling, H., Edge, A. C., & Henry, J. P. 2001, *ApJ*, 553, 668
 Ebeling, H., Ma, C. J., Kneib, J.-P., et al. 2009, *MNRAS*, 395, 1213
 Fabian, A. C., Sanders, J. S., Taylor, G. B., et al. 2006, *MNRAS*, 366, 417
 Ferrari, C., Intema, H. T., Orrù, E., et al. 2011, *A&A*, 534, L12
 George, E. M., Reichardt, C. L., Aird, K. A., et al. 2015, *ApJ*, 799, 177
 Gilfanov, M. R., & Syunyaev, R. A. 1984, *SvAL*, 10, 137
 Gilmour, R., Best, P., & Almaini, O. 2009, *MNRAS*, 392, 1509
 Gitti, M., Ferrari, C., Domainko, W., Feretti, L., & Schindler, S. 2007a, *A&A*, 470, L25
 Gitti, M., Piffaretti, R., & Schindler, S. 2007b, *A&A*, 475, 441
 Glenn, J., Bock, J. J., Chattopadhyay, G., et al. 1998, Proc. SPIE, 3357, 326
 Golovich, N., Dawson, W. A., Wittman, D., et al. 2016, *ApJ*, 831, 110
 Haig, D. J., Ade, P. A. R., Aguirre, J. E., et al. 2004, Proc. SPIE, 5498, 78
 Hasselfield, M., Hilton, M., Marriage, T. A., et al. 2013, *JCAP*, 7, 8
 Jewell, P. R., & Prestage, R. M. 2004, Proc. SPIE, 5489, 312
 Johnson, R. E., Zuhone, J., Jones, C., Forman, W. R., & Markevitch, M. 2012, *ApJ*, 751, 95
 Kartaltepe, J. S., Ebeling, H., Ma, C. J., & Donovan, D. 2008, *MNRAS*, 389, 1240
 Keisler, R., Reichardt, C. L., Aird, K. A., et al. 2011, *ApJ*, 743, 28
 Kitayama, T., Komatsu, E., Ota, N., et al. 2004, *PASJ*, 56, 17
 Kitayama, T., Ueda, S., Takakuwa, S., et al. 2016, *PASJ*, 68, 88
 Komatsu, E., Matsuo, H., Kitayama, T., et al. 2001, *PASJ*, 53, 57
 Korngut, P. M., Dicker, S. R., Reese, E. D., et al. 2011, *ApJ*, 734, 10
 Kravtsov, A. V., & Borgani, S. 2012, *ARA&A*, 50, 353
 LaRoque, S. J., Bonamente, M., Carlstrom, J. E., et al. 2006, *ApJ*, 652, 917
 LaRoque, S. J., Joy, M., Carlstrom, J. E., et al. 2003, *ApJ*, 583, 559
 Lau, E. T., Nagai, D., Kravtsov, A. V., & Zentner, A. R. 2011, *ApJ*, 734, 93
 Lemze, D., Postman, M., Genel, S., et al. 2013, *ApJ*, 776, 91
 Limousin, M., Ebeling, H., Richard, J., et al. 2012, *A&A*, 544, A71
 Ma, C.-J., Ebeling, H., & Barrett, E. 2009, *ApJL*, 693, L56
 Mann, A. W., & Ebeling, H. 2012, *MNRAS*, 420, 2120
 Mantz, A., Allen, S. W., Rapetti, D., & Ebeling, H. 2010, *MNRAS*, 406, 1759
 Mantz, A. B., Allen, S. W., Morris, R. G., & Schmidt, R. W. 2016, *MNRAS*, 456, 4020
 Markevitch, M., Gonzalez, A. H., Clowe, D., et al. 2004, *ApJ*, 606, 819
 Markevitch, M., & Vikhlinin, A. 2007, *PhR*, 443, 1
 Markwardt, C. B. 2009, in ASP Conf. Ser. 411, Astronomical Data Analysis Software and Systems XVIII, ed. D. A. Bohlender, D. Durand, & P. Dowler (San Francisco, CA: ASP), 251
 Mason, B. S., Dicker, S. R., Korngut, P. M., et al. 2010, *ApJ*, 716, 739
 Maughan, B. J., Jones, C., Forman, W., & van Speybroeck, L. 2008, *ApJS*, 174, 117
 Mauskopf, P. D., Horner, P. F., Aguirre, J., et al. 2012, *MNRAS*, 421, 224
 McDonald, M., Benson, B. A., Vikhlinin, A., et al. 2014, *ApJ*, 794, 67
 McNamara, B. R., & Nulsen, P. E. J. 2007, *ARA&A*, 45, 117
 McNamara, B. R., Rafferty, D. A., Bîrzan, L., et al. 2006, *ApJ*, 648, 164
 McNamara, B. R., Russell, H. R., Nulsen, P. E. J., et al. 2014, *ApJ*, 785, 44
 Miranda, M., Sereno, M., de Filippis, E., & Paolillo, M. 2008, *MNRAS*, 385, 511
 Morandi, A., & Cui, W. 2014, *MNRAS*, 437, 1909
 Morandi, A., Nagai, D., & Cui, W. 2013, *MNRAS*, 436, 1123
 Morandi, A., Sun, M., Forman, W., & Jones, C. 2015, *MNRAS*, 450, 2261
 Mroczkowski, T., Bonamente, M., Carlstrom, J. E., et al. 2009, *ApJ*, 694, 1034
 Mroczkowski, T., Dicker, S., Sayers, J., et al. 2012, *ApJ*, 761, 47
 Nagai, D., Kravtsov, A. V., & Vikhlinin, A. 2007, *ApJ*, 668, 1
 Nagai, D., & Lau, E. T. 2011, *ApJL*, 731, L10
 Navarro, J. F., Frenk, C. S., & White, S. D. M. 1997, *ApJ*, 490, 493
 Nelson, K., Lau, E. T., & Nagai, D. 2014, *ApJ*, 792, 25
 Newman, A. B., Treu, T., Ellis, R. S., et al. 2009, *ApJ*, 706, 1078
 O'Dea, K. P., Quillen, A. C., O'Dea, C. P., et al. 2010, *ApJ*, 719, 1619
 Ota, N., Murase, K., Kitayama, T., et al. 2008, *A&A*, 491, 363
 Peng, F., & Nagai, D. 2009, *ApJ*, 693, 839

- Plagge, T. J., Marrone, D. P., Abdulla, Z., et al. 2013, *ApJ*, 770, 112
- Planck Collaboration, Ade, P. A. R., Aghanim, N., et al. 2013, *A&A*, 558, C2
- Pointecouteau, E., Giard, M., Benoit, A., et al. 1999, *ApJL*, 519, L115
- Pointecouteau, E., Giard, M., Benoit, A., et al. 2001, *ApJ*, 552, 42
- Postman, M., Coe, D., Benítez, N., et al. 2012, *ApJS*, 199, 25
- Pratt, G. W., Arnaud, M., Piffaretti, R., et al. 2010, *A&A*, 511, A85
- Reese, E. D., Carlstrom, J. E., Joy, M., et al. 2002, *ApJ*, 581, 53
- Reichardt, C. L., Shaw, L., Zahn, O., et al. 2012, *ApJ*, 755, 70
- Reichardt, C. L., Stalder, B., Bleem, L. E., et al. 2013, *ApJ*, 763, 127
- Romero, C. E., Mason, B. S., Sayers, J., et al. 2015, *ApJ*, 807, 121
- Rumsey, C., Olamaie, M., Perrott, Y. C., et al. 2016, *MNRAS*, 460, 569
- Sayers, J., Czakon, N. G., Bridge, C., et al. 2012, *ApJL*, 749, L15
- Sayers, J., Czakon, N. G., Mantz, A., et al. 2013a, *ApJ*, 768, 177
- Sayers, J., Golwala, S. R., Ameglio, S., & Pierpaoli, E. 2011, *ApJ*, 728, 39
- Sayers, J., Mroczkowski, T., Czakon, N. G., et al. 2013b, *ApJ*, 764, 152
- Schindler, S., Guzzo, L., Ebeling, H., et al. 1995, *A&A*, 299, L9
- Schindler, S., Hattori, M., Neumann, D. M., & Boehringer, H. 1997, *A&A*, 317, 646
- Schmidt, R. W., & Allen, S. W. 2007, *MNRAS*, 379, 209
- Schmidt, R. W., Allen, S. W., & Fabian, A. C. 2001, *MNRAS*, 327, 1057
- Shaw, L. D., Nagai, D., Bhattacharya, S., & Lau, E. T. 2010, *ApJ*, 725, 1452
- Siegel, S. R., Sayers, J., Mahdavi, A., et al. 2016, arXiv:1612.05377
- Smith, G. P., Ebeling, H., Limousin, M., et al. 2009, *ApJL*, 707, L163
- Sunyaev, R. A., & Zel'dovich, Y. B. 1972, *CoASP*, 4, 173
- Umetsu, K., Medezinski, E., Nonino, M., et al. 2012, *ApJ*, 755, 56
- van Weeren, R. J., Ogrea, G. A., Jones, C., et al. 2017, *ApJ*, 835, 197
- van Weeren, R. J., Röttgering, H. J. A., Brügger, M., & Cohen, A. 2009, *A&A*, 505, 991
- Vikhlinin, A., Kravtsov, A., Forman, W., et al. 2006, *ApJ*, 640, 691
- Young, A. H., Mroczkowski, T., Romero, C., et al. 2015, *ApJ*, 809, 185
- Zitrin, A., Broadhurst, T., Barkana, R., Rephaeli, Y., & Benítez, N. 2011, *MNRAS*, 410, 1939
- Zitrin, A., Broadhurst, T., Rephaeli, Y., & Sadeh, S. 2009, *ApJL*, 707, L102
- Zitrin, A., Fabris, A., Merten, J., et al. 2015, *ApJ*, 801, 44
- Zitrin, A., Moustakas, J., Bradley, L., et al. 2012a, *ApJL*, 747, L9
- Zitrin, A., Rosati, P., Nonino, M., et al. 2012b, *ApJ*, 749, 97